

Article

Synthesis and Characterization of Zn–Organic Frameworks Containing Chitosan as a Low-Cost Inhibitor for Sulfuric-Acid-Induced Steel Corrosion: Practical and Computational Exploration

Mohamed Gouda ^{1,*}, Mai M. Khalaf ^{1,2} , Kamal Shalabi ³ , Mohammed A. Al-Omair ¹ and Hany M. Abd El-Lateef ^{1,2,*} 

- ¹ Department of Chemistry, College of Science, King Faisal University, P.O. Box 400, Al-Hofuf 31982, Saudi Arabia; mmkali@kfu.edu.sa (M.M.K.); alomair@kfu.edu.sa (M.A.A.-O.)
² Chemistry Department, Faculty of Science, Sohag University, Sohag 82524, Egypt
³ Chemistry Department, Faculty of Science, Mansoura University, Mansoura 11432, Egypt; dr-kamal@mans.edu.eg
* Correspondence: mgoudaam@kfu.edu.sa (M.G.); hmahmed@kfu.edu.sa or hany_shubra@science.sohag.edu.eg (H.M.A.E.-L.)

Abstract: In this work, a Zn–benzenetricarboxylic acid (Zn@H₃BTC) organic framework coated with a dispersed layer of chitosan (CH/Zn@H₃BTC) was synthesized using a solvothermal approach. The synthesized CH/Zn@H₃BTC was characterized by Fourier transform infrared spectroscopy (FTIR), field emission scanning electron microscope (FESEM), thermal gravimetric analysis (TGA), and Brunauer, Emmett, and Teller (BET) surface area. The microscopic observation and the analysis of the BET surface area of CH/Zn@H₃BTC nanocomposites indicated that chitosan plays an important role in controlling the surface morphology and surface properties of the Zn@H₃BTC. The obtained findings showed that the surface area and particle size diameter were in the range of 80 m² g^{−1} and 800 nm, respectively. The corrosion protection characteristics of the CH/Zn@H₃BTC composite in comparison to pristine chitosan on duplex steel in 2.0 M H₂SO₄ medium determined by electrochemical (*E* vs. time, PDP, and EIS) approaches exhibited that the entire charge transfer resistance of the chitosan- and CH/Zn@H₃BTC-composite-protected films on the duplex steel substrate was comparatively large, at 252.4 and 364.8 Ω cm² with protection capacities of 94.1% and 97.8%, respectively, in comparison to the unprotected metal surface (*R*_p = 20.6 Ω cm²), indicating the films efficiently protected the metal from corrosion. After dipping the uninhabited and protected systems, the surface topographies of the duplex steel were inspected by FESEM. We found the adsorption of the CH/Zn@H₃BTC composite on the metal interface obeys the model of the Langmuir isotherm. The CH/Zn@H₃BTC composite revealed outstanding adsorption on the metal interface as established by MD simulations and DFT calculations. Consequently, we found that the designed CH/Zn@H₃BTC composite shows potential as an applicant inhibitor for steel protection.

Keywords: metal organic framework (MOF); chitosan; duplex steel; solvothermal method; corrosion protection; theoretical study



Citation: Gouda, M.; Khalaf, M.M.; Shalabi, K.; Al-Omair, M.A.; El-Lateef, H.M.A. Synthesis and Characterization of Zn–Organic Frameworks Containing Chitosan as a Low-Cost Inhibitor for Sulfuric-Acid-Induced Steel Corrosion: Practical and Computational Exploration. *Polymers* **2022**, *14*, 228. <https://doi.org/10.3390/polym14020228>

Academic Editor: Oleg V. Surov

Received: 2 December 2021

Accepted: 2 January 2022

Published: 6 January 2022

Publisher's Note: MDPI stays neutral with regard to jurisdictional claims in published maps and institutional affiliations.



Copyright: © 2022 by the authors. Licensee MDPI, Basel, Switzerland. This article is an open access article distributed under the terms and conditions of the Creative Commons Attribution (CC BY) license (<https://creativecommons.org/licenses/by/4.0/>).

1. Introduction

The steel alloys utilized in oil and petroleum manufacturing can vary from API N80 mild steel, J55, and L80, to corrosion-resistant alloys with high chromium content, such as austenitic-ferritic steel, amended martensitic 13.0% Cr steel (Super-13), and duplex 20–22% Cr steel [1–3]. Corrosion is a serious problem affecting steel alloys in harsh solutions, particularly in acidic media, which hinders the lifetime and the related abilities of these alloys, and can even result in severe accidents. Additionally, the rust released from steel into

the environment imposes a heavy ecological burden. Thus, researchers have focused on improving the deterioration of C steel in various harsh solutions.

Corrosion inhibitors are one of the experimental approaches used for protection against corrosion, specifically in acidic solutions [4–8]. The various inhibitors that have been applied and test industrially as corrosion additives [9–12] are those are low- or non-toxic are currently better than the materials used in the recent past such as glucose, gellan gum, carboxymethyl, hydroxypropyl cellulose [9,11], xanthan gum [10], and chitosan-g-PEG [12]. Recently, the research in the area of eco-friendly or green corrosion inhibitors has been directed toward fabricating inexpensive, efficient composites that have no or minimal environmental impact [13,14].

Organic bridging ligands and metal nodes are utilized to create metal–organic frameworks (MOFs) [15]. MOFs are gaining popularity among researchers because of their ease of functionalization, variable pore diameters, and large surface area [16,17]. MOFs are potential candidates for a variety of applications, including gas separation and storage [18], fuel cells [19], solar cells [20], catalysis [21], sensors [22], electrical devices [23], drug delivery [24], and others, due to their beneficial features.

Chitosan is made by deacetylating chitin via alkaline hydrolysis [25]. Chitosan is a biodegradable, biocompatible, nontoxic, and structurally stable biopolymer [26]. Chitosan-coated MOFs preserve their crystalline structure and high porosity and do not producing toxicity issues compared to pure MOFs [27]. MOFs' chemical and colloidal stabilities may also be improved via surface modification.

As a result of the accuracy of MOF construction, scientists have continue to develop applications of MOF compounds and have accomplished many outcomes, but comparatively fewer studies have applied them for corrosion inhibition [28,29]. The MOF structure has large pores; consequently, sequences of composite compounds are fabricated using various groups on graphene oxide to coordinate with the MOF materials with the purpose of obstructing the characteristics of graphene, providing the MOF with corrosion protection ability, thereby inhibiting the impact of corrosion on steel [30–32]. The anticorrosion properties of MOF-decorated graphene oxide nano-platforms were investigated; the findings showed that the graphene oxide/zeolitic imidazolate framework-8 loaded composite material has respectable protection capacity [33]. A benzotriazole/MOF/tetraethyl orthosilicate/graphene oxide nanocomposite was prepared and its anticorrosive action was inspected. The findings confirmed that the fabricated nanocomposite combined into the protective films presented strong anticorrosion characteristics [34].

To overcome the problems due to the large pores in MOF skeletons, in this study, the prepared MOFs material was coated with chitosan as a dispersed layer. We synthesized chitosan containing a Zn@1,3,5-benzene tricarboxylic acid framework via the solvothermal method and characterized it by FTIR, SEM, TGA, and BET surface area. Then, the corrosion protection capacities of the prepared CH/Zn@H₃BTC were compared to those of pristine chitosan for duplex steel in sulfuric acid solution by electrochemical methods (EIS, PDP, and E_{OCP} vs. time) with concentrations ranging from 20 to 200 ppm. To examine the adsorption kinetics of CH and CH/Zn@H₃BTC on the metal substrate, some models of the adsorption isotherms were examined. The changes in the morphology of the corroding metal substrate in the blank and inhibited systems were detected by FESEM. Monte Carlo simulations and DFT calculations were concluded to understand the corrosion protection process.

2. Experimental Method

2.1. Materials

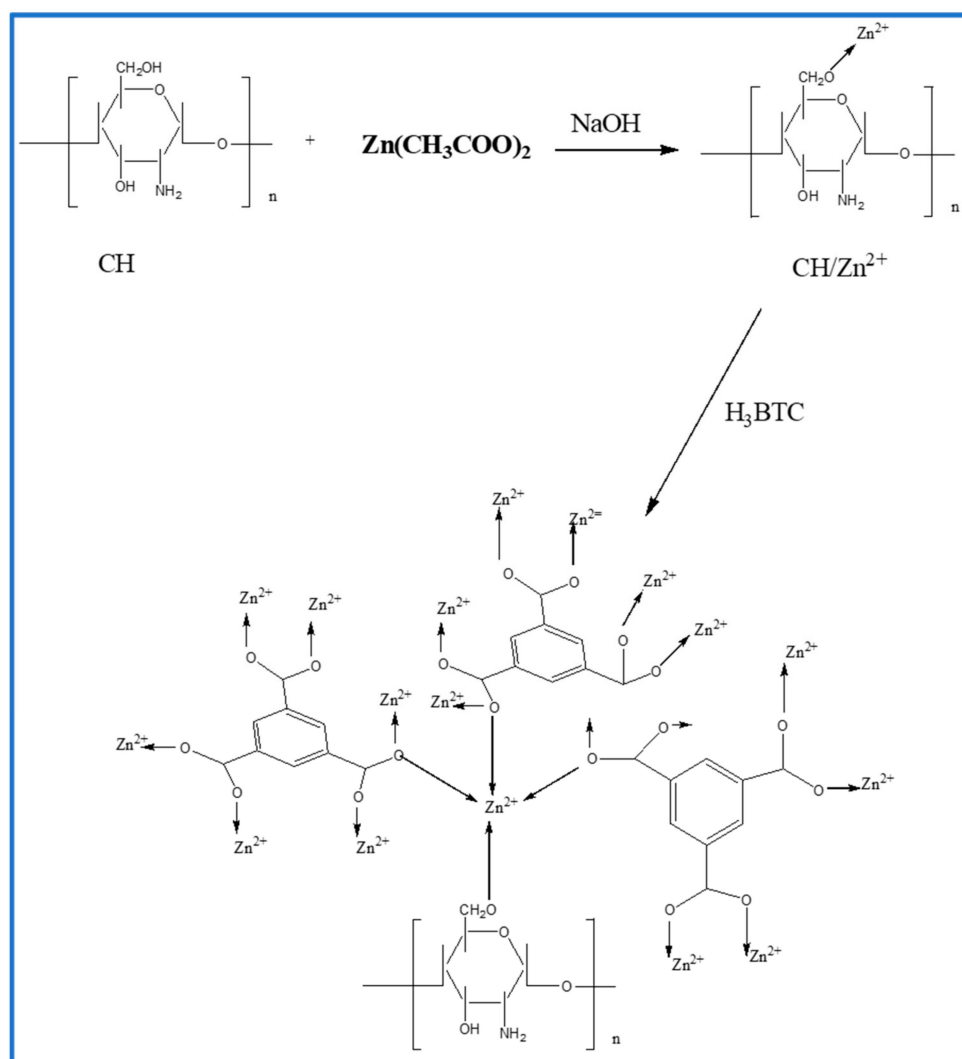
Chitosan with a high molecular weight with 85% deacetylation was purchased from Sigma-Aldrich Co. (St. Louis, MO, USA). Zn acetate dihydrate (ACS reagent, $\geq 98\%$) and 1,3,5-benzen tricarboxylic acid (98%) were purchased from Sigma-Aldrich Co. (St. Louis, MO, USA). Ethanol and other chemical reagents were purchased from Merck Co. (Darmstadt, Germany).

Duplex steel (D steel) was utilized during the experimentations. The chemical configuration of D steel is (wt.%): 0.012 C, 0.56 Si, 0.81 Mn, 0.019 P, 0.001 S, 22.15%Cr, 0.163 N, and 3.12 MO, and the rest is Fe. Before the corrosion protection a test, the working electrode (D steel) was abraded with a SiC paper in a sequence from 600 to 1500 grit. The samples were washed methodically with bidistilled H₂O and degreased with acetone.

A stock solution of analytical-grade sulfuric acid (98%) was used to prepare an aqueous solution of the corrosive medium (2.0 M H₂SO₄) by the dilution process.

2.2. Preparation of CH/Zn@H₃BTC Composite Beads

Scheme 1 depicts the CH/Zn@H₃BTC composite bead preparation method. To make a homogenous solution, 1.0 g CH and 1.5 g zinc acetate were mixed in 100 mL acetic acid solution (1%, *v/v*) and stirred at 550 rpm for 4 h. The solution was then put into a 1.0 M NaOH solution. The CH/Zn²⁺ particles were removed after 15 min and rinsed three times with deionized water to remove the excess NaOH before being immersed in an aqueous solution containing 2.6 g (0.15 mol) 1,3,5-benzenetricarboxylic acid (H₃BTC). Zn²⁺ reacted with H₃BTC at this point, forming Zn@H₃BTC composite beads. The CH/Zn@H₃BTC composite beads were then washed three times with deionized water, immersed in isopropanol, and freeze-dried for 12 h to produce CS/Zn@H₃BTC composite beads.



Scheme 1. Proposed schematic synthesis of chitosan/Zn@1,3,5-benzenetricarboxylic acid (CH/Zn@H₃BTC).

2.3. Materials' Characterization

A Fourier transform infrared (FTIR) spectrometer (Spectrometer Model FTIR-8400S, Shimadzu, Japan) was utilized in the range of 400.0 to 4000.0 cm^{-1} for the determination of the functional groups in the samples. Thermogravimetric analysis (TGA) was completed using a thermogravimetric device (Model-Q 500- Lukens Drive, TA Instruments, New Castle, DE, USA) to measure the thermal steadiness of CH/Zn@H₃BTC. Field emission scanning electron microscopy (FESEM) (Model-JOEL-JXA-840-Tokyo 196-8558, Japan) was used to inspect the surface morphology of CH, Zn@H₃BTC, and CH/Zn@H₃BTC.

2.4. Specific Surface Area Studies

The surface area of CH/Zn@H₃BTC were calculated using the Brunauer–Emmett–Teller (BET) method. The N₂ adsorption–desorption was measured on a programmed gas sorption analyzer (Ji Nan RunZhi Technology, Shanghai, China). The prepared CH/Zn@H₃BTC was outgassed for 4.0 to 6.0 h and N₂ adsorption–desorption isotherms were evaluated at 77.35 K by the volumetric method, which represents extra adsorption isotherms [35].

2.5. Corrosion Protection Evaluation

The Gamry Galvanostat/Potentiostat/ZRA electrochemical workstation (Gamry Instruments, Warminster, PA, USA), according to the ASTM standard approach [36], was used to complete all electrochemical tests in a 3-electrode cell at 50 °C and under non-stirring conditions. A D steel substrate covered in an epoxy container (an efficient area of 1.0 cm^2) was used as the operational electrode, Pt sheet was employed as the counter electrode, and silver/silver chloride (KCl_{sat.}) was utilized as the reference electrode. Before the electrochemical tests, the working electrode (D steel) was immersed in the blank and inhibited corrosive medium for 45 min to steady the open circuit potential (E_{ocp}). Potentiodynamic polarization (PDP) was performed with a potential range of -250 to $+250$ mV vs. E_{ocp} at a scanning rate of 0.2 mV s^{-1} . Electrochemical impedance spectroscopy (EIS) was completed in the frequency range of 0.1 Hz to 100 kHz with a sine amplitude of 10 mV at E_{ocp} . Corrosion current density (j_{cor}) was determined by the extrapolation of anodic and cathodic Tafel lines to corrosion potential (E_{cor}) [6].

2.6. Surface Exploration

The surface topographies of the D steel substrates after 24 h of soaking in 2.0 M H₂SO₄ medium without and with 200 ppm of CH and CH/Zn@H₃BTC at 323 K were scanned by an SEM device (JSM-6610 LV model) at an accelerating voltage of 20 kV. A surface investigation of the pristine polished D steel was also performed for comparison.

2.7. Theoretical Approaches

The correlation between the inhibition efficiencies and the molecular structure of the inhibitor was detected via theoretical calculations [37]. Computerized studies were performed by Accelrys Materials Studio 7.0 with the DMol³ module for DFT computations and with the adsorption locator module for MC simulations. Monomer structures of CH and CH/Zn@H₃BTC were optimized in DFT calculations by applying the GGA/BLYP function with the DNP foundation set and COSMO solving controls [37]. For MC simulations, the suitable adsorption configurations for the monomer structures of CH and CH/Zn@H₃BTC molecules on Fe (1 1 0) exterior were achieved via the adsorption locator module based on Monte Carlo investigations to assess the protection potency of the examined inhibitors [38]. The adsorption of the examined components, water particles, and exterior of Fe (1 1 0) was determined via a simulation box ($32.27 \times 32.27 \times 50.18 \text{ \AA}^3$) through the appointed COMPASS force field [38].

3. Results and Discussions

3.1. Characterization Analysis

3.1.1. FTIR

Figure 1A,B shows the FTIR of blank CH and Zn@H₃BTC/CH; the spectra show that the absorption bands of the carbonyl (C=O) and hydroxyl (–OH) groups. The peak observed at 1622 cm^{–1} matches the C=O stretching band and the peak at 1375 cm^{–1} was assigned as the stretching vibration the C–O bond, demonstrating the deprotonation of the carboxylate group (from H₃BTC) and coordination with the Zn(II) metal ion to form ZnO₃(BTC)₂. We observed the characteristic peaks of the MOF at 1578 cm^{–1}, corresponding to the C=C of the aromatic ring, and at 1521 cm^{–1}, corresponding to the C=O of the strong carbonyl group. In addition, a characteristic peak at 1375 cm^{–1} was observed due to the presence of the carboxyl group. Due to the presence of carboxylate, no peak was observed at 1722 cm^{–1} due to the shift of the –OH group. This is mainly the reason that lengthy conjugate π -bonds are created from the carboxylate formed from carboxyl anion, thus creating the two-oxygen-atom equivalent. Furthermore, a strong characteristic peak was observed at 729 cm^{–1}, corresponding to ZnO. According to Scheme 1, the zinc ion has four coordinated bonds, three of which are with H₃BTC and the other with the chitosan molecule. Every H₃BTC binds six zinc ions.

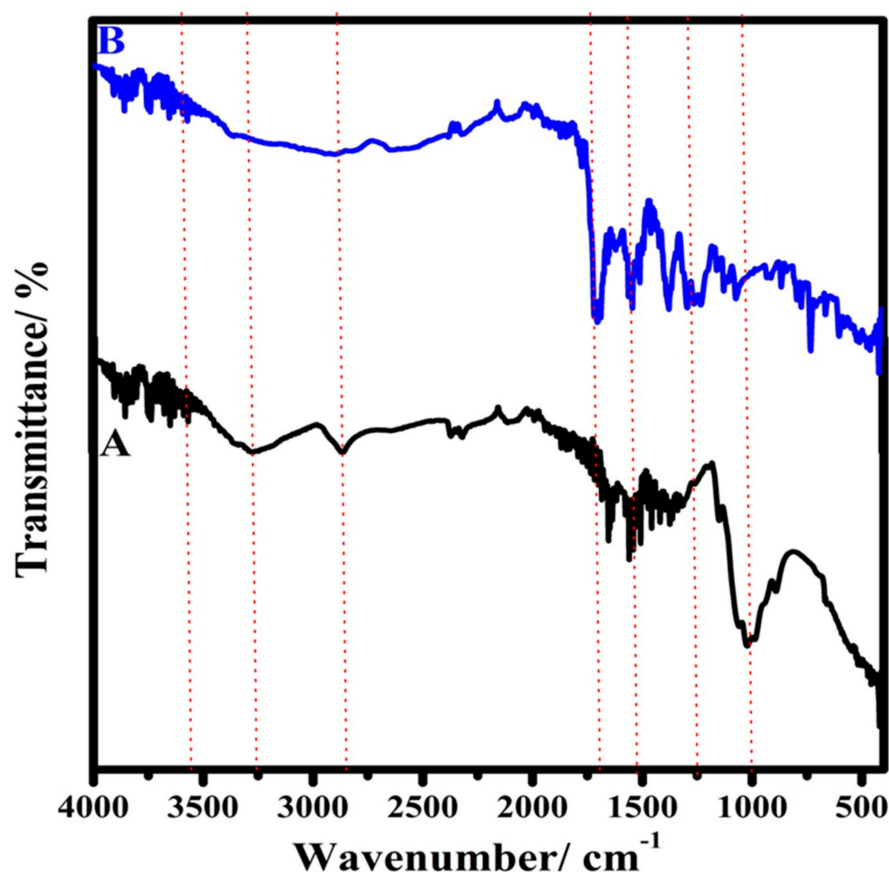


Figure 1. FTIR spectra of (A) CH and (B) CH/Zn@H₃BTC.

3.1.2. Thermal Analysis

Figure 2 displays the thermogravimetric measurement of CH and CH/Zn@H₃BTC, illustrating the thermal stability and features of the thermal degradation of CH polymer and its composite. The overall weight loss of CH and CH/Zn@H₃BTC, recorded with heating over the temperature range of RT–700 °C, were 40% and 60%, respectively. The results showed that the weight loss process and evolution of the CH and CH/Zn@H₃BTC structures occurred through three steps stages of decomposition.

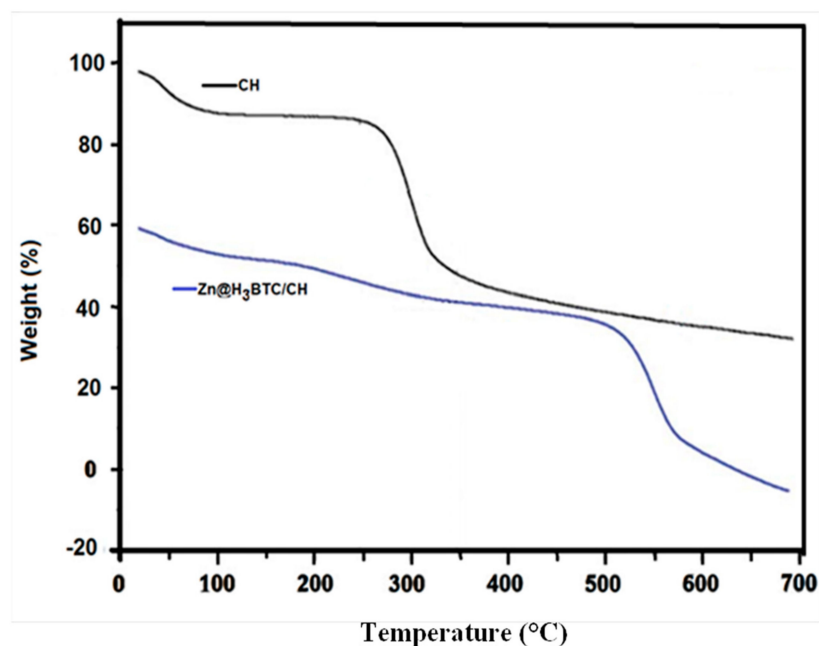


Figure 2. Thermogravimetric diagram of CH and CH/Zn@H₃BTC.

Based on the steps and the weight loss values for the CH sample and its composite, we assigned the first step below 120 °C to the loss of the adsorbed and included water and/or organic molecules; a ΔW of 10% was exhibited. This was followed by two steps from 200 to 380 °C, and a final step above 400 °C. The weight loss change for the CH sample for the second stage ($\Delta W = \sim 25\%$) and for the last stage ($\Delta W = \sim 5\%$) might have occurred due to the breakdown of chitosan molecules. The weight loss change for the CH/Zn@H₃BTC sample was lower in the second stage ($\Delta W = \sim 7\%$) than in the last stage ($\Delta W = \sim 43\%$). The weight loss values assigned for the last stage of the CH sample ($\Delta W = \sim 5\%$) and the CH/Zn@H₃BTC sample ($\Delta W = \sim 43\%$) confirm the insertion of Zn into the organic framework. Furthermore, the TGA curve of the CH/Zn@H₃BTC had a larger weight loss compared to that of CH, thus confirming the improved interfacial binding of Zn into the chitosan matrix.

3.1.3. FESEM

FESEM was used to inspect the surface morphology of CH, Zn@H₃BTC, and CH/Zn@H₃BTC. The morphological features of CH, which has a smooth surface, are presented in Figure 3a. Figure 3b depicts a microscopic view of the geometry of Zn@H₃BTC powder, which has an irregular polyhedral structure with a pore size range of 500–800 nm. Figure 3c shows the porous morphology of CH/Zn@H₃BTC, which is characterized by micron-sized homogeneously dispersed spherical pores. The presence of chitosan should have aided the formation of smooth porous spheres. For CH/Zn@H₃BTC, however, the morphology was altered to a more finely dispersed mesoporous structure. The structure of Zn@H₃BTC remained constant in the absence of CH. The prepared CH/Zn@H₃BTC ultimately condensed in the presence of CH due to CH's cohesiveness. This showed that CH has a minimal influence on the morphology of Zn@H₃BTC and that the surface of Zn@H₃BTC was successfully capped with CH.

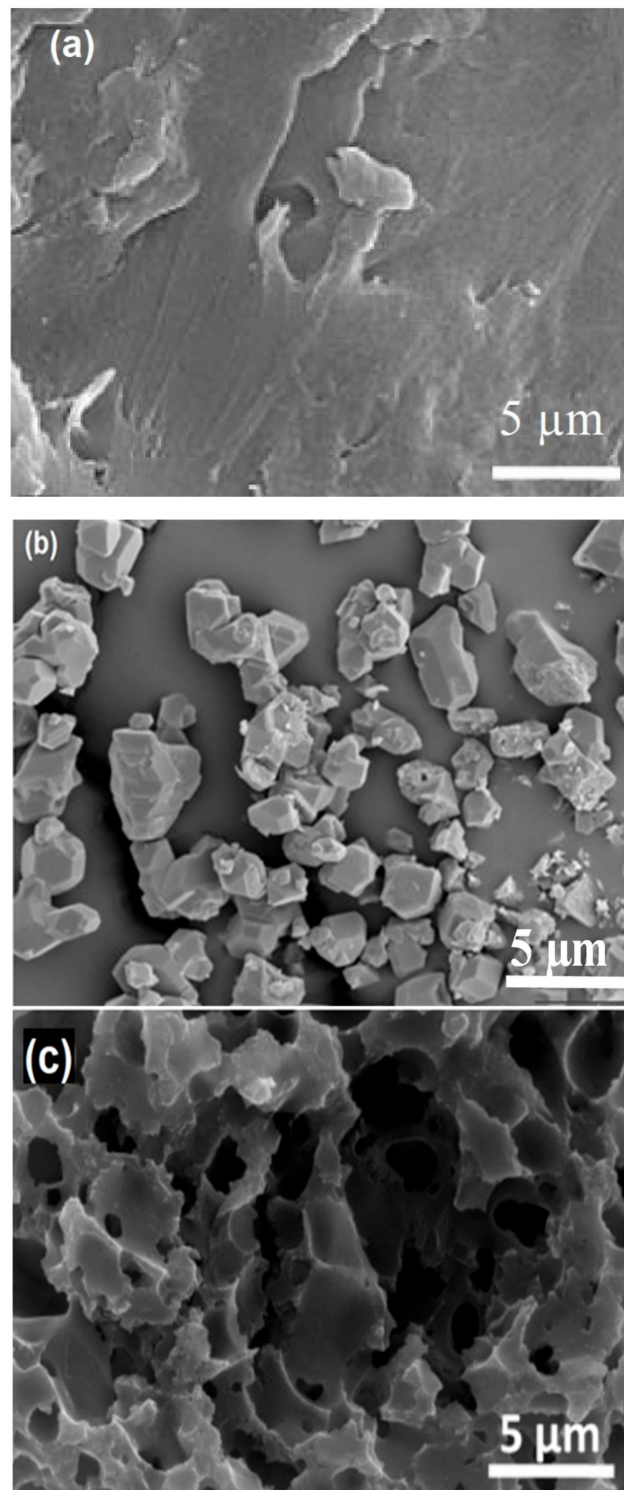


Figure 3. SEM of the CH (a), Zn@H₃BTC (b), and CH/Zn@H₃BTC (c).

3.1.4. BET Analysis

The N₂ adsorption–desorption isotherms of CH/Zn@H₃BTC are shown in Figure 4A. The results demonstrated that the first inflection point is at $p/p_0 < 2$, which indicates the completion of monolayer adsorption. As the pressure increased, the adsorption of the second layers occurred. The number of adsorption layers is limitless at saturated vapor pressure so the adsorption isotherm is characteristic of type II. According to the multipoint BET technique, the surface area of CH/Zn@H₃BTC was estimated as 80 m²/g.

In addition to the pore size distribution of CH/Zn@H₃BTC, Figure 4B displays a mean pore diameter of 22.5 nm, which confirmed the mesoporosity of the CH composite. This reasonable mesoporous feature would help the CH/Zn@H₃BTC composite to easily diffuse and adsorb on steel substrates to hence act as a potential corrosion inhibitor.

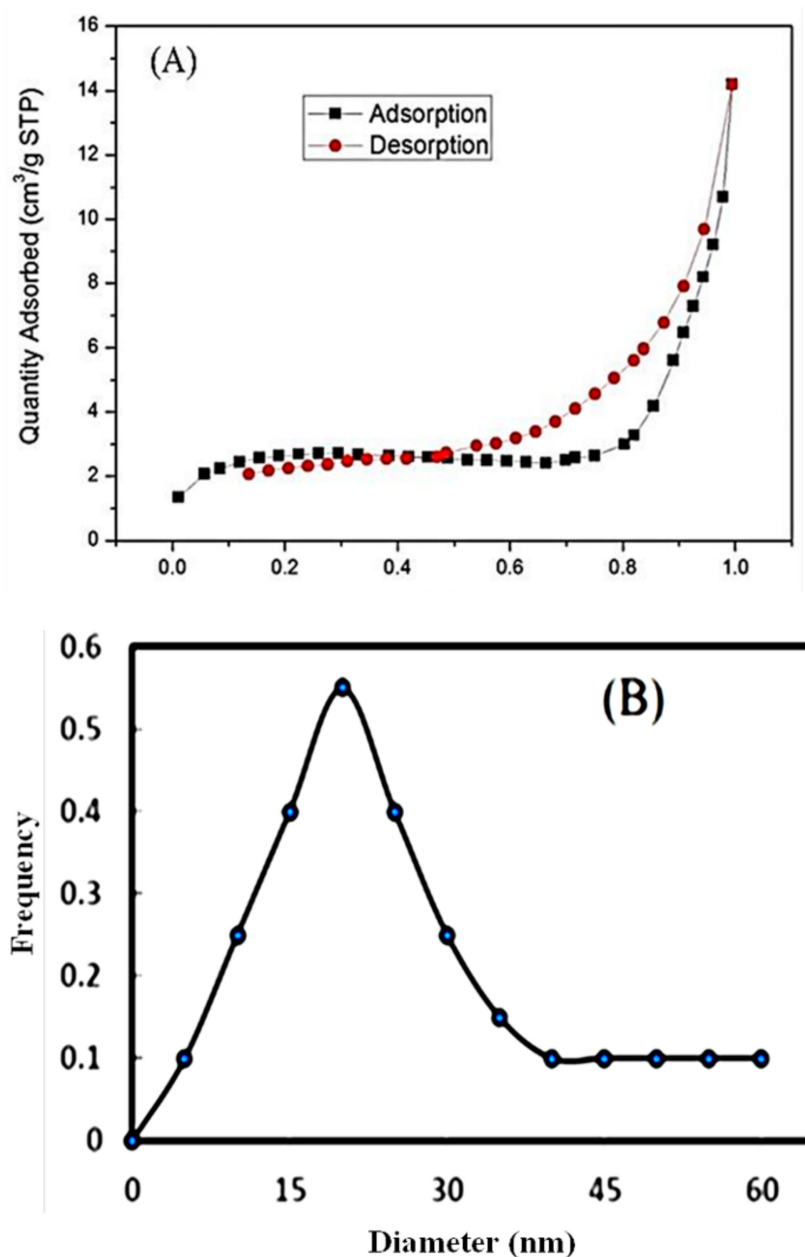


Figure 4. N₂ adsorption-desorption isotherm at 77.35 K, for CH/Zn@H₃BTC (A) and the pore size distribution of CH/Zn@H₃BTC (B).

3.2. Corrosion Protection Evaluation

3.2.1. $E_{OCP}-t$ Profiles

A steady potential lacking an external current was applied on the duplex steel's interface for EIS and PP experiments. Figure 5 displays the profiles of E_{OCP} (vs. a Ag/AgCl electrode) in 2.0 M sulfuric acid medium without and with 200 ppm of CH and CH/Zn@H₃BTC as a function of dipping time at 323 K. For the blank and solutions containing 200 ppm (optimum dose) of CH and CH/Zn@H₃BTC, various immersion times were necessary to attain a stable E_{OCP} value. It can be observed from Figure 5 that 50 min was sufficient to

attain a stable E_{OCP} , so this time was consequently employed as the exposure time before PP and EIS experiments.

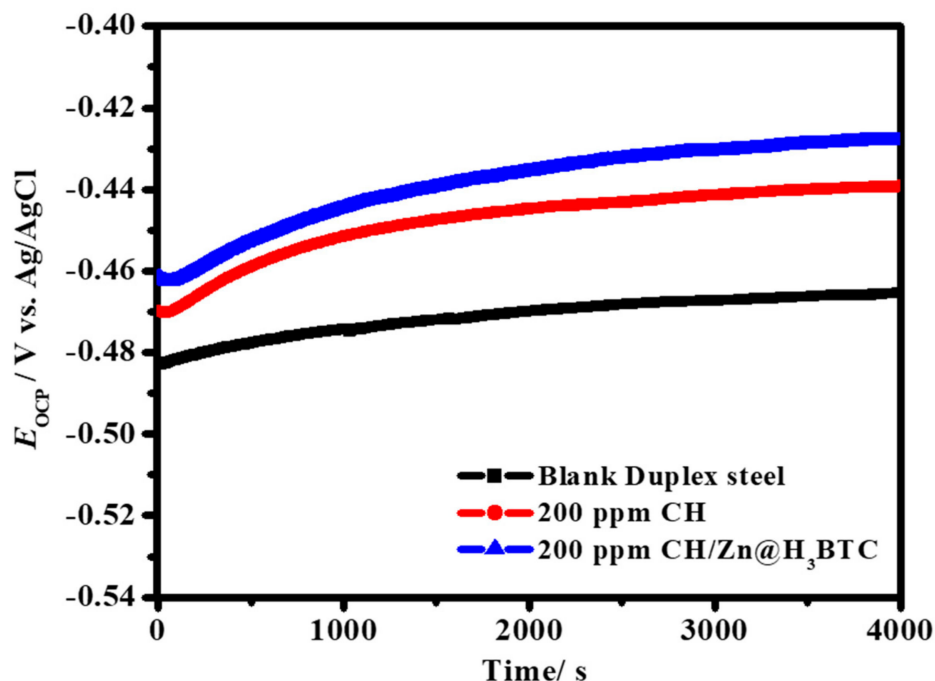


Figure 5. E_{OCP} versus t profiles for duplex steel in a 2.0 M sulfuric acid medium without and with 200 ppm CH and CH/Zn@H₃BTC.

3.2.2. PDP Studies and Comparative Evaluation

Figure 6 presents the Tafel plots of duplex steel in 2.0 M sulfuric acid medium without and with various concentrations of CH (Figure 6A) and CH/Zn@H₃BTC (Figure 6B) at 323 K. In Figure 6, anodic and cathodic Tafel lines move clearly to lower current values with the addition of CH and CH/Zn@H₃BTC, due to the insertion of CH and CH/Zn@H₃BTC in the corrosive solution inhibiting the hydrogen ions' reduction and reducing the anodic dissolution of the metal. Furthermore, the decreases in the density of the cathode current values were more noticeable than those of the anode, which showed that the adsorption of CH and CH/Zn@H₃BTC on the metal surface efficiently prevents hydrogen evolution at the cathode side.

To understand the mechanism of the inhibition process of CH and CH/Zn@H₃BTC on duplex steel in 2.0 M H₂SO₄, the important PP parameters such as corrosion voltage (E_{COR}), corrosion current density (j_{COR}), and anodic and cathodic Tafel slopes (β_a and β_c) are recorded in Table 1. By extrapolation of the anodic and cathodic lines, the E_{COR} and j_{COR} values were obtained. The inhibition capacity ($\eta_{PP}/\%$) is calculated by Equation (1) as follows [39]:

$$\eta_{PP}/\% = \left(\frac{j_{COR,0} - j_{COR,i}}{j_{COR,0}} \right) \times 100 = \theta \times 100 \quad (1)$$

where $j_{COR,0}$ and $j_{COR,i}$ are j_{COR} with and without CH and CH/Zn@H₃BTC in 2.0 M H₂SO₄, respectively.

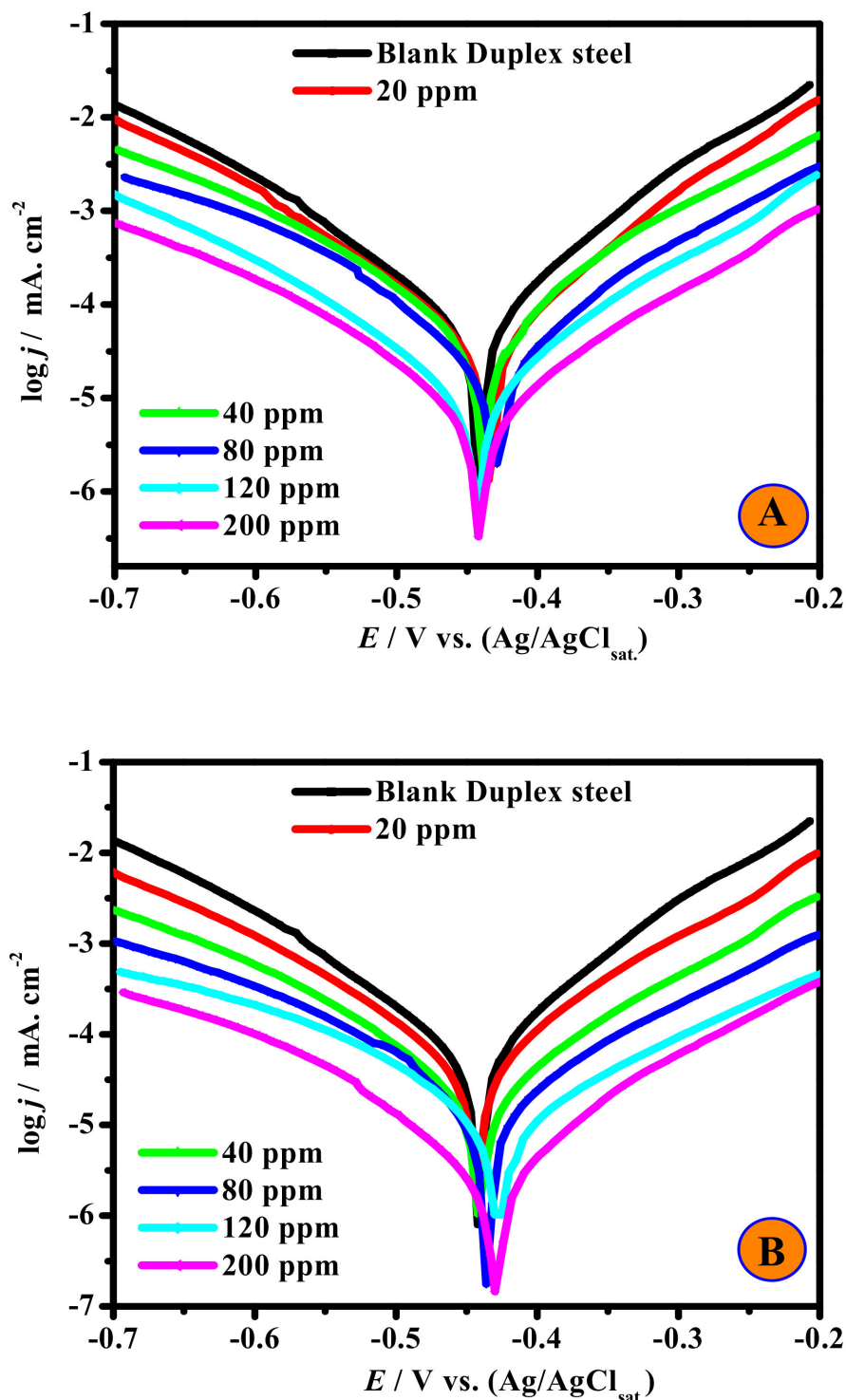


Figure 6. Tafel profiles for duplex steel at 323 K in 2.0 M H_2SO_4 without and with various concentrations of (A) CH and (B) CH/Zn@H₃BTC.

Table 1 shows that the β_a and β_c values were different for the different concentrations CH and CH/Zn@H₃BTC and the blank system, demonstrating that CH and CH/Zn@H₃BTC can control the anode and cathode reactions [40]. Moreover, the change in the $(\Delta E_{\text{cor}}) E_{\text{cor}}$ values was less than 0.085 V vs. Ag/AgCl in all cases, showing that CH and CH/Zn@H₃BTC are mixed-kind inhibitors [41]. The j_{cor} value declined from 1137.7 $\mu\text{A cm}^{-2}$ for the uninhibited system to 713.33 and 613.22 $\mu\text{A cm}^{-2}$ with the addition of 20 ppm of CH and CH/Zn@H₃BTC, respectively, which further diminished to 67.12 and 25.02 μA

cm^{-2} for 200 ppm CH and CH/Zn@H₃BTC, respectively. The protection ability of CH and CH/Zn@H₃BTC, as calculated by Equation (1), are 37.3% and 46.1%, and 94.1% and 97.8% at concentrations of 20 and 200 ppm, respectively. By comparing the findings with those of previously reported compounds [42,43], we found the protection efficacy of CH and CH/Zn@H₃BTC is clearly stronger. The improved protection capability might be attributed to the bonded functional chitosan and benzene ring owing to the extra donor–acceptor attractions among the empty d orbitals of iron atoms and the π electrons.

Table 1. PDP parameters achieved for duplex steel in 2.0 M H₂SO₄ solution in the absence and presence of various concentrations of CH and CH/Zn@H₃BTC at 50 °C.

Inhibitors Code	C _{inh} ppm by weight	E _{cor} V vs. Ag/AgCl	j _{cor} μA cm ⁻² ±SD	β _a mV dec ⁻¹ ±SD	-β _c mV dec ⁻¹ ±SD	θ	ζ _{PP} %
Blank	0.0	-0.441	1137.7 ± 71	70.7 ± 5.2	138.8 ± 11.6	-	-
	20	-0.433	713.33 ± 51.4	81.5 ± 3.4	146.4 ± 10.1	0.373	37.3
	40	-0.437	550.68 ± 32.2	78.1 ± 5.7	147.9 ± 9.7	0.516	51.6
CH	80	-0.429	293.52 ± 19.3	79.8 ± 4.1	143.7 ± 6.8	0.742	74.2
	120	-0.442	120.59 ± 9.8	81.2 ± 7.1	140.3 ± 8.5	0.894	89.4
	200	-0.437	67.12 ± 5.3	83.9 ± 2.9	153.4 ± 6.3	0.941	94.1
	20	-0.442	613.22 ± 45.6	84.6 ± 3.8	152.5 ± 7.6	0.461	46.1
	40	-0.441	427.77 ± 23.9	86.1 ± 4.8	153.6 ± 12.2	0.624	62.4
CH/Zn@H ₃ BTC	80	-0.434	145.62 ± 10.2	79.2 ± 3.9	149.2 ± 13.4	0.872	87.2
	120	-0.428	71.67 ± 6.4	87.5 ± 7.5	150.4 ± 9.8	0.937	93.7
	200	-0.427	25.02 ± 1.5	82.3 ± 7.1	153.7 ± 7.4	0.978	97.8

3.2.3. EIS Studies

The corrosion performance of duplex steel in a 2.0 molar sulfuric acid medium both with and without the prepared CH and CH/Zn@H₃BTC composite was examined by EIS at 50 ± 1 °C at E_{OCP}. The kinetics of the electrode, surface characteristics, and mechanism were attained from the EIS graphs [44]. The Nyquist plots of duplex steel in the investigated corrosive medium at 323 K without and with various doses of CH polymer and CH/Zn@H₃BTC composite are depicted in Figure 7A,B. We observed that the Nyquist profiles were imperfect capacitive loops (Figure 7), which showed that the metal dissolution was controlled by the charge shift route in the studied corrosive medium [45]. The capacitive loop (Figure 7) displayed a nonperfect arc in a 2.0 M H₂SO₄ medium owing to the inhomogeneity and roughness of the duplex steel interface.

After investigating the Nyquist profile shape, we found that the Nyquist diagrams exhibited a depressed capacitive loop in the higher-frequency (HF) area and a minor inductive loop in the lower-frequency (LF) area, demonstrating the existence of a Faradic process on the permitted metal sites. The capacitive loop in the HF area was recognized as time-continuous for the double electric layer and the charge transfer process. However, the inductive loop at the LF area was ascribed to the recreation of intermediates regulating the corrosion process due to species adsorption, for instance, FeSO₄ [46], or inhibitor molecules [47] on the metal interface. It may also be related to the re-dissolution of the oxide film in the lower-frequency range [48]. The capacitive loop diameter with the CH polymer and CH/Zn@H₃BTC composite was larger than that of the blank system, and increased with increasing dose. This showed that the resistance of the inhibited steel surface increased with the inhibitor concentration. The diameter of the semi-circle followed the order of CH/Zn@H₃BTC composite < CH polymer under the same conditions, which showed that the most active adsorption film on the electrode interface was produced with CH/Zn@H₃BTC composite in 2.0 M sulfuric acid medium, which powerfully obstructed the effects of corrosion of the acid medium.

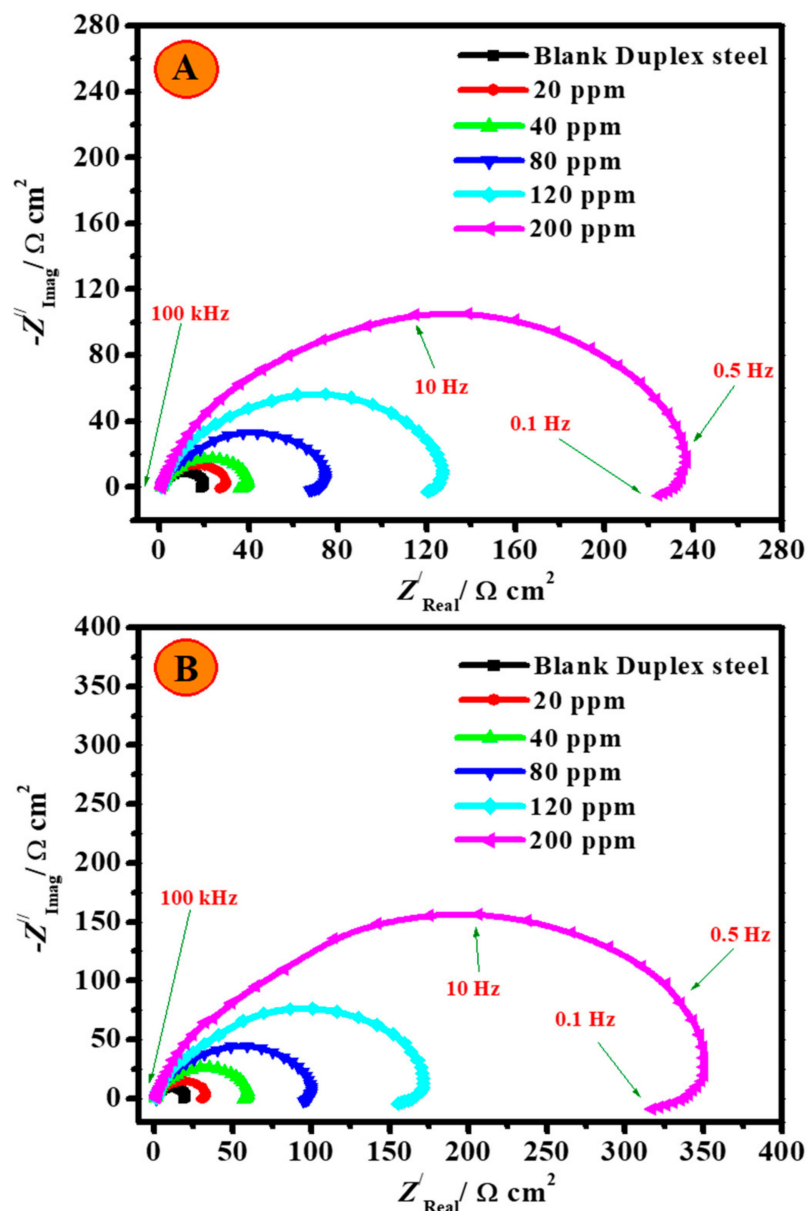


Figure 7. Nyquist plots for duplex steel at 323 K in 2.0 M H_2SO_4 with and without various concentrations of (A) CH and (B) CH/Zn@ H_3BTC .

Bode profiles for duplex steel at 323 K in 2.0 M H_2SO_4 without and with various concentrations of CH and CH/Zn@ H_3BTC are presented in Figures 8 and 9. A single time constant was detected in the Bode profiles, demonstrating that the duplex steel corrosion in the studied corrosive medium was predominantly organized by a charge transfer route. At the electrode/medium interface, the charge sharing on the electrode cross was well-ordered by electrons; however, it was orderly by the ions on the medium side. Subsequently, there were many more ions than electrons. A slight difference in capacitance was observed compared to a perfect capacitor at the steel/electrolyte interface [49]. As revealed in Figures 8 and 9, the phase angle and impedance modulus values considerably increased with increasing doses of CH and CH/Zn@ H_3BTC . The impedance modulus value increased by two orders of magnitude and the phase angle increased to 82° when the optimum dose of CH/Zn@ H_3BTC was used (200 ppm), which showed that CH/Zn@ H_3BTC adsorption efficiently impedes the corrosion of duplex steel in 2.0 M H_2SO_4 [50].

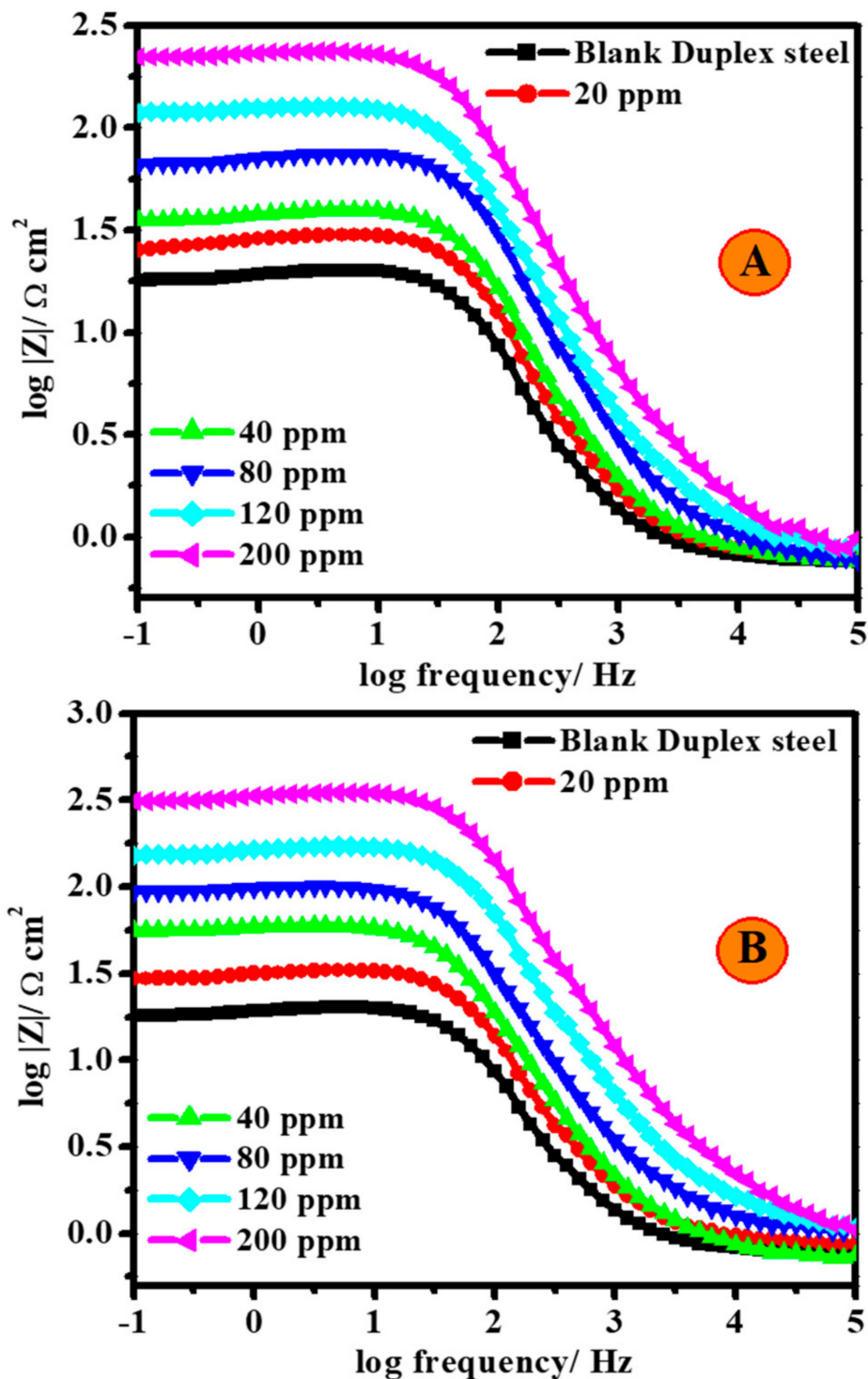


Figure 8. Bode profiles for duplex steel at 323 K in 2.0 M H₂SO₄ with and without various concentrations of (A) CH and (B) CH/Zn@H₃BTC.

Nyquist profiles and fitted plots (—) for duplex steel in blank 2.0 M H₂SO₄ solution and in the presence of 200 ppm of CH at 50 °C are presented in Figure 10A,B, respectively, and an electrical equivalent circuit (EEC) is presented in the Figure 10 inset. The EEC was used to measure the electrolyte impedance (R_s), the resistance of charge transfer (R_{ct}), the constant phase element (CPE), the inductance resistor (R_L), and the inductance (L), in

addition to the film resistance (R_f) in the case of the inhibited system. The CPE impedance is computed through the following formula [51]:

$$Z_{CPE} = \frac{1}{Y_0(j\omega)^n} \tag{2}$$

where Y_0 is the CPE constant, j is the $\sqrt{-1}$, ω is the angular frequency, and n is the deviation factor. The capacitance of double layer (C_{dl}) was utilized rather than CPE because it could more precisely fit the impedance parameters. The C_{dl} value was calculated by the Brug formula [52]:

$$C_{dl} = Y_0^{\frac{1}{n}} \left(\frac{1}{R_s} + \frac{1}{R_{ct}} \right)^{1-\frac{1}{n}} \tag{3}$$

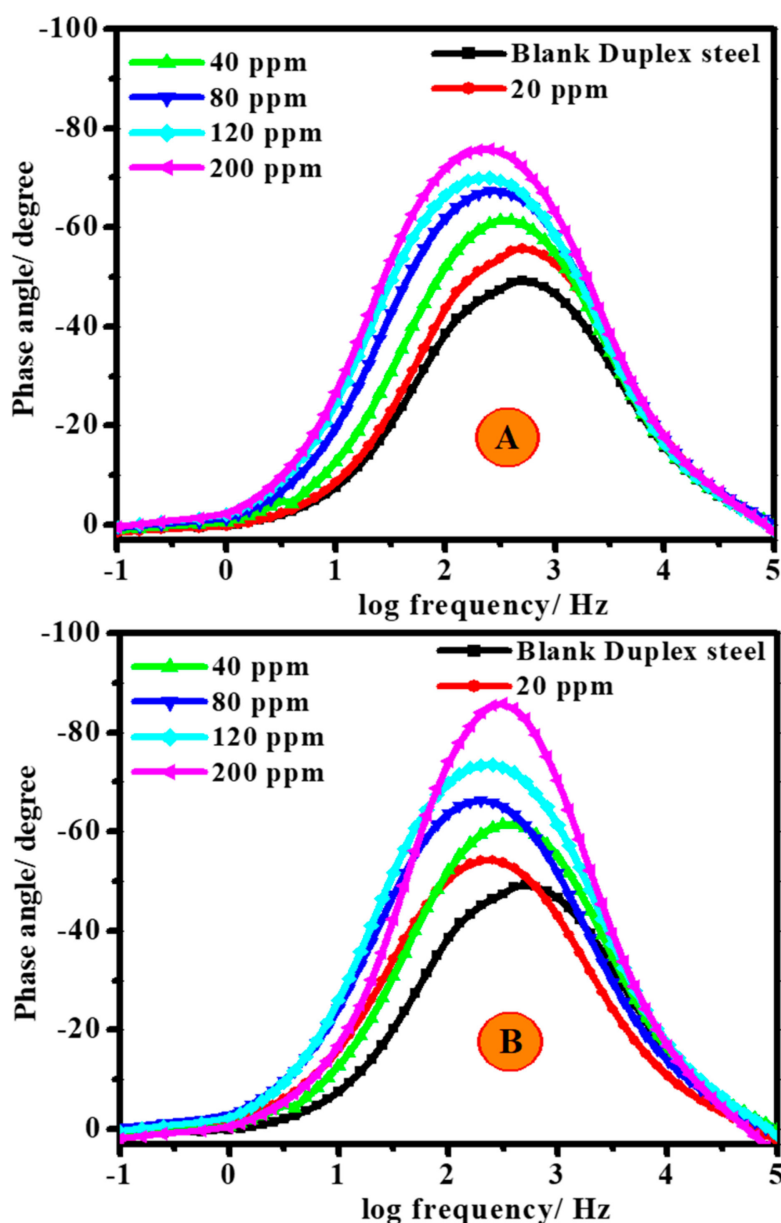


Figure 9. Bode phase profiles for duplex steel at 323 K in 2.0 M H_2SO_4 with and without various concentrations of (A) CH and (B) CH/Zn@H₃BTC.

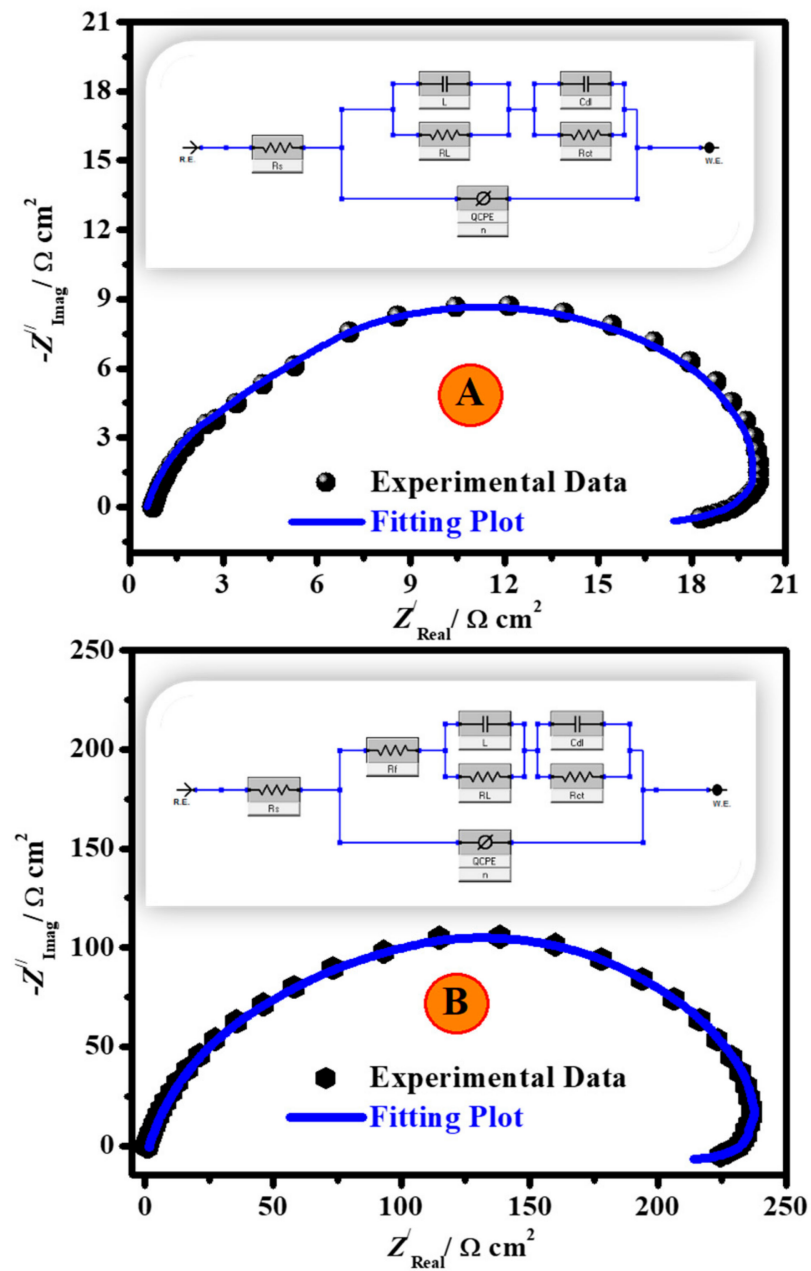


Figure 10. Nyquist profiles and fitted plots of duplex steel in blank 2.0 M H₂SO₄ solution (A) and in the presence of 200 ppm of CH (B) at 50 °C. Inset, equivalent circuit used to fit the EIS findings.

The protection ability ($\eta\%$) was computed from the resistance of the charge transfer (R_{ct}) values as follows [53]:

$$\eta/\% = \left(\frac{R_{ct}^i - R_{ct}^f}{R_{ct}^i} \right) \times 100 \tag{4}$$

where R_{ct}^i and R_{ct}^f represent the R_{ct} for the free and inhibited systems, respectively. The fit of the EEC was evaluated by the chi-square (χ^2) value [53]. The attained χ^2 values (3.91×10^{-4} to 5.48×10^{-4}) in Table 2 show an appropriate fit to the EEC. The R_{ct} value increased from 20.6 to 30.4 and 33.3 $\Omega \text{ cm}^2$ when the CH and CH/Zn@H₃BTC doses reached 20 ppm, respectively. The values of R_{ct} reached the highest values at 252.4 and 364.8 $\Omega \text{ cm}^2$ at 200 ppm for CH and CH/Zn@H₃BTC, respectively, demonstrating the decline in the rate of steel corrosion. Consequently, $\eta\%$ values of 91.8% and 94.3% were obtained for CH and

CH/Zn@H₃BTC, respectively, demonstrating the promising corrosion protection ability of CH polymer and CH/Zn@H₃BTC composite for duplex steel in the investigated corrosive medium. Due to the appropriate CH polymer and CH/Zn@H₃BTC composite adsorption at the electrode/electrolyte interface, the pre-adsorbed H₂O molecules were increasingly replaced by the inhibitor components with a small dielectric constant. Accordingly, C_{dl} decreased with the increase in CH polymer and CH/Zn@H₃BTC composite dose according to the subsequent Equation (5):

$$C_{dl} = \left(\frac{\epsilon\epsilon_0}{d} \right) \times S \quad (5)$$

where ϵ_0 and ϵ are the constants of a vacuum and the local dielectric, respectively; d represents the double film thickness; and S is the active electrode area. The adsorption of CH polymer and CH/Zn@H₃BTC composite on the duplex steel interface decreased ϵ and increased d . Consequently, C_{dl} was lower for the duplex steel in the inhibited system. The continual increase in R_{ct} and the decrease in C_{dl} also showed that the adsorption film of CH polymer and CH/Zn@H₃BTC composite was inclined to be compact and uniform. Based on their adsorption, the value of n regularly increased and nearly reached unity. Higher n values were detected for the sample in the acidic solution containing CH polymer and CH/Zn@H₃BTC inhibitors. This indicated a comparatively homogeneous and smooth surface owing to the inhibitor adsorption. In summary, the EIS differences in the protection competencies agree with that achieved from the PP method.

Table 2. EIS parameters achieved for duplex steel in in 2.0 M H₂SO₄ solution in the absence and presence of various concentrations of CH and CH/Zn@H₃BTC at 50 °C.

Additive Codes	C_{inh} ppm	R_e Ω cm ²	R_{ct} Ω cm ² ±SD	C_{dl} F cm ⁻² × 10 ⁻⁶	R_p Ω cm ² ±SD	R_L Ω cm ²	L H cm ²	Q_{CPE}		$\chi^2 \times 10^{-4}$	ζ_E %
								Y_0 μΩ ⁻¹ s ^{n} cm ⁻²	n		
2.0 M H ₂ SO ₄	0.0	0.69	20.6 ± 1.6	540.5	9.6	18.2	11.82	133.93	0.739	3.91	–
CH	20	0.83	30.4 ± 2.1	161.8	14.2	26.9	29.91	38.27	0.829	4.93	32.2
	40	0.99	41.1 ± 3.2	134.3	19.1	35.7	36.25	32.42	0.845	4.96	49.8
	80	1.21	75.4 ± 4.7	84.8	35.3	66.7	57.15	20.13	0.841	4.99	72.6
	120	1.42	129.3 ± 9.4	44.4	62.2	120.1	107.53	10.62	0.849	5.25	84.1
	200	1.78	252.4 ± 16.8	26.9	117.8	220.9	178.45	6.37	0.865	5.06	91.8
CH/Zn@H ₃ BTC	20	0.83	33.3 ± 1.4	121.5	15.7	29.9	40.38	28.77	0.849	5.48	38.1
	40	0.91	61.9 ± 3.6	82.8	29.5	56.6	58.26	19.61	0.862	5.44	66.7
	80	1.26	102.8 ± 6.2	67.7	49.3	94.8	71.79	15.84	0.897	5.18	79.9
	120	1.85	177.1 ± 16.9	37.6	82.7	155.5	130.75	8.92	0.856	5.14	88.3
	200	2.24	364.8 ± 23.1	14.7	168.3	312.7	244.02	3.72	0.889	5.32	94.3

3.3. Adsorption Considerations, Thermodynamic Research, and Corrosion Mitigation Mechanism

Corrosion mitigation properties were attained through to the adsorption of inhibitor species onto the electrode interface to form a compact defensive layer and protect the electrode from the acidic solution. Alternatively, the adsorbed inhibitor species may integrate with the oxide film on the steel (rust) and chemically interact to yield an additional protecting interface system by altering the construction of the layer. The adsorption processes of inhibitor molecule occur directly based on donor–acceptor attractions among the comparatively insecure bound electrons, for instance, in anions, inhibitor molecules, and/or the polymeric materials that have π electrons, or free coupled electrons with unoccupied d orbitals of the Fe atoms on the metallic interface. Some factors, including the size of the inhibitor molecule, the number of efficient groups, the polarity that influences

the development of a robust bond, or the adsorption rate of inhibitor molecules onto a metallic interface, can disturb the inhibition and/or adsorption processes [54].

Some isotherm adsorption models, such as Frumkin, Temkin, Langmuir, El-Awady Flory–Huggins, and so on, were applied to fit PP the findings. These data showed that the Langmuir model displayed a respectable linear association with the experimental PP results. The isotherm of the Langmuir adsorption model is defined as follows [55]:

$$\frac{C_{in}}{\theta} = \frac{1}{K_{ad}} + C_{in} \tag{6}$$

where C_{in} is the inhibitor dose, K_{ad} is the constant of adsorptive stability, and θ is the part of covered surface. C_{in}/θ versus C_{in} produced a straight line with the regression coefficient ($R^2 = 0.9972$ and 0.9985 for CH and CH/Zn@H₃BTC, respectively) and the slope was close to unity ($S = 0.855$ and 0.884 for CH and CH/Zn@H₃BTC, respectively) at the investigated temperature, as revealed in Figure 11. These findings demonstrated that the adsorption of CH and CH/Zn@H₃BTC on metal surfaces is agreement with the Langmuir isotherm model. The free energy of standard adsorption (ΔG_{ads}^0) is attained by the subsequent equation [55]:

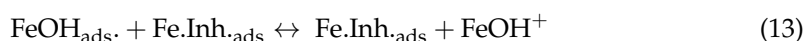
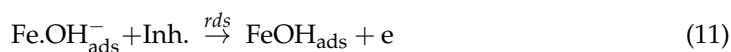
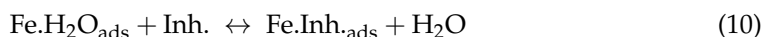
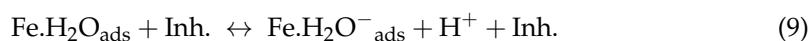
$$\Delta G_{ads}^0 = -2.303RT \log(1 \times 10^6 K_{ads}) \tag{7}$$

where R represents the universal gas constant, T is the absolute temperature, and 1×10^6 is the H₂O concentration. The greater the K_{ad} value ($K_{ad} = 0.026$ and 0.041 L/g for CH and CH/Zn@H₃BTC, respectively), the larger the area of covered surface, and the better the anticorrosion film of CH and CH/Zn@H₃BTC on the electrode interface. The computed values of G_{ads}^0 were found to be -27.3 and -28.5 kJ g⁻¹ for CH and CH/Zn@H₃BTC, respectively. The negative values of G_{ads}^0 suggested the spontaneous adsorption of CH and CH/Zn@H₃BTC at the electrode/electrolyte interface [56].

In this study, the G_{ads}^0 values were found to be greater than -20 kJ g⁻¹ and smaller than -40 kJ g⁻¹, showing that the mechanism of adsorption of the CH and CH/Zn@H₃BTC on duplex steel in 2.0 M sulfuric medium was mainly based on chemical and physical adsorption [57].

Consequently, physisorption might occur owing to electrostatic attractions among the protonated inhibitor molecule and FeSO₄²⁻ species. The chemical adsorption of the CH polymer and CH/Zn@H₃BTC composite on the metallic interface might occur through donor–acceptor attractions between the π electrons of O (and/or N) fragments and the empty d orbitals of iron atoms. Furthermore, with the attraction of the chitosan chain to the metal interface, polymer long chains correspondingly play a significant role in the inhibition and adsorption performance.

The mechanism in acidic media comprising two adsorbed intermediates was suggested for the hindrance of iron anodic dissolution in the presence of an inhibitor, as follows [58]:



where Inh. Represents the inhibitor molecule.

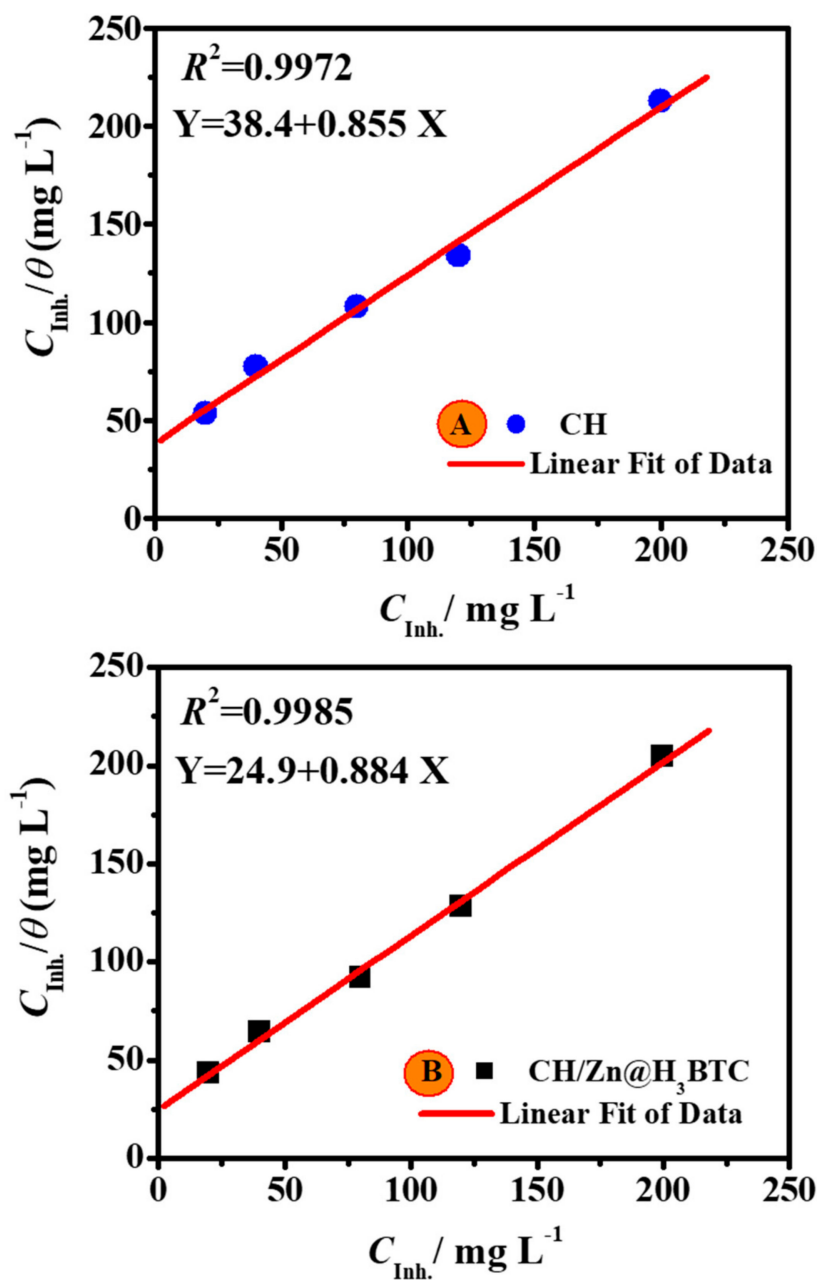


Figure 11. Plots of the Langmuir isotherm extracted from Tafel plots at 323 K in 2.0 M H₂SO₄ with and without various concentrations of (A) CH and (B) CH/Zn@H₃BTC.

3.4. Surface Topography Exploration

In order to understand the inhibition characteristics of the CH polymer and CH/Zn@H₃BTC composite, the surface topology of duplex steel was investigated. The FE-SEM images of the electrode interface after 24 h of submersion in 2.0 M sulfuric acid both with and without 200 ppm of CH polymer and CH/Zn@H₃BTC composite are presented in Figure 12A–D. We observed big pits and deep cracks on the electrode surface (Figure 12B) in the solution without inhibitors, which was significantly different from the pristine metal, as shown in Figure 12A. This showed that duplex steel extremely corroded in the 2.0 M sulfuric medium. However, the steel surface showed a comparatively smoother surface morphology with 200 ppm CH polymer and CH/Zn@H₃BTC composite, which was comparable to the pristine surface (Figure 12C,D). In comparison, in the presence of 200 ppm CH/Zn@H₃BTC composite (Figure 12D), the metal interface displayed much

less corrosion, i.e., a much smoother surface. Furthermore, these findings showed that the CH polymer and CH/Zn@H₃BTC composite adsorbed on the electrode surface to produce a defensive layer that prohibited corrosion by the acidic solution. Therefore, the electrode was well-shielded by the CH polymer and CH/Zn@H₃BTC composite in the studied acidic medium.

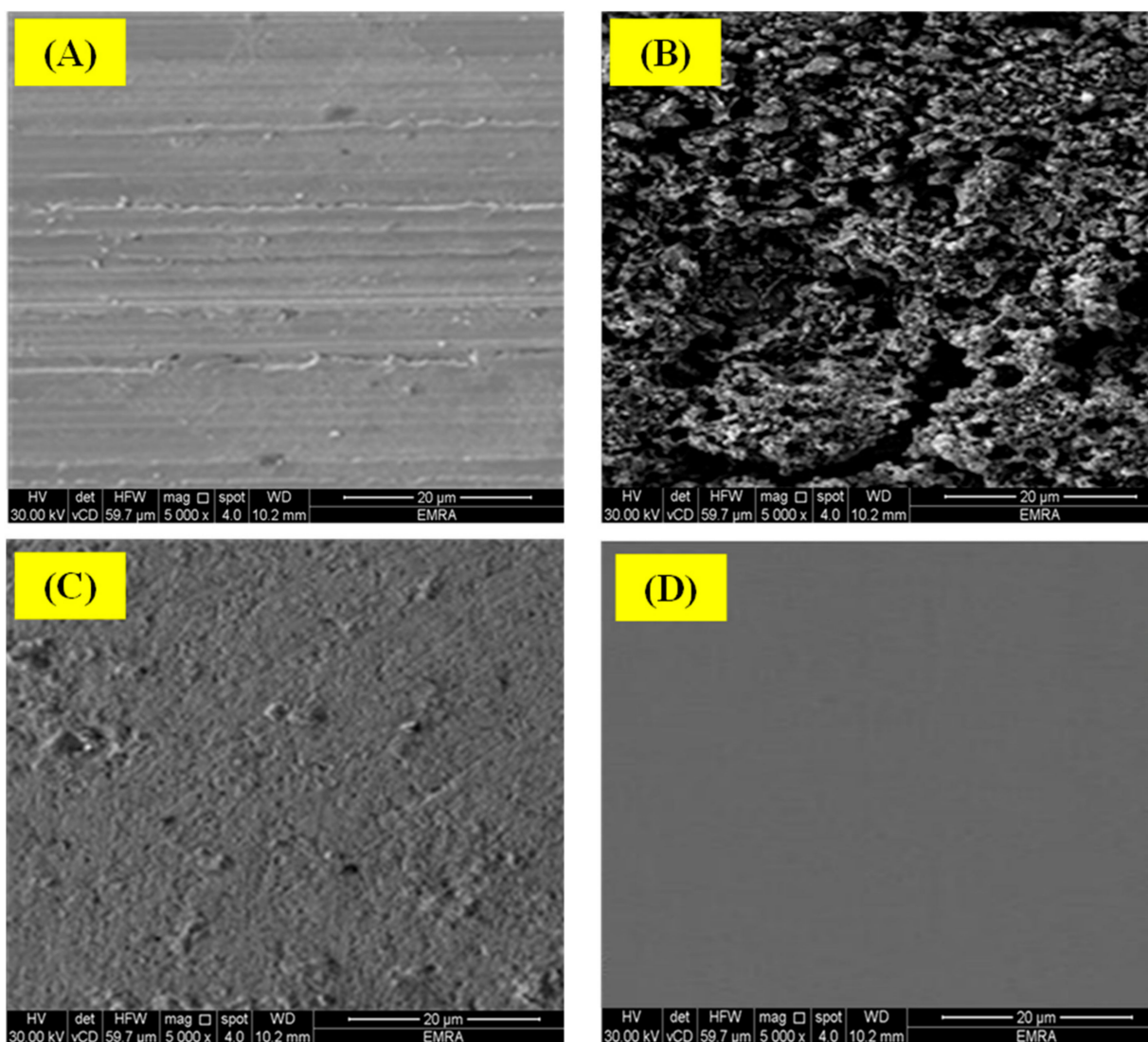


Figure 12. FE-SEM images of the pristine duplex steel (A) substrates after 24 h dipping in blank 2.0 M H₂SO₄ solutions without (B) and with of 200 ppm CH polymer (C) and CH/Zn@H₃BTC composite (D).

3.5. DFT Studies

DFT computations were performed to investigate the interaction between the active centers on CH and CH/Zn@H₃BTC molecules and steel surfaces. The optimized constructions, HOMO and LUMO orbitals, for CH and CH/Zn@H₃BTC molecules are shown in Figure 13, and the quantum chemical variables are listed in Table 3. Based on the FMO hypothesis, the provider and receiver capability of the inhibitor molecule in the inhibitor/metal exterior interaction are assigned by HOMO and LUMO energies [59]. In this way, a molecule that has large E_{HOMO} and low E_{LUMO} values is deemed to be an efficient corrosion inhibitor. As presented in Table 3, CH/Zn@H₃BTC had a higher E_{HOMO} value (−9.11 eV) than CH (−5.00 eV). As presented in Figure 13, for inhibitor molecules, it is obvious that the HOMO level was situated on the N and O atoms; thus, these positions

were chosen for the electrophilic study on the steel exterior. Such justifications approve the ability of CH and CH/Zn@H₃BTC to be adsorbed on the steel exterior, thus demonstrating the anticorrosion ability, in agreement with the experimental outcomes. Moreover, the E_{LUMO} value was -8.57 eV for CH/Zn@H₃BTC (Table 3), which is less than that of CH (0.81 eV), in agreement with experimental data; however, CH/Zn@H₃BTC showed greater inhibition potency than CH. Additionally, the energy difference (ΔE) is a vital indicator of the prohibition ability of molecules, i.e., it increases as the ΔE value decreases [60]. As demonstrated in Table 3, CH/Zn@H₃BTC had a lower ΔE value (0.55 eV) than CH (5.80 eV), which indicates the greater tendency of CH/Zn@H₃BTC to be adsorbed on steel's exterior.

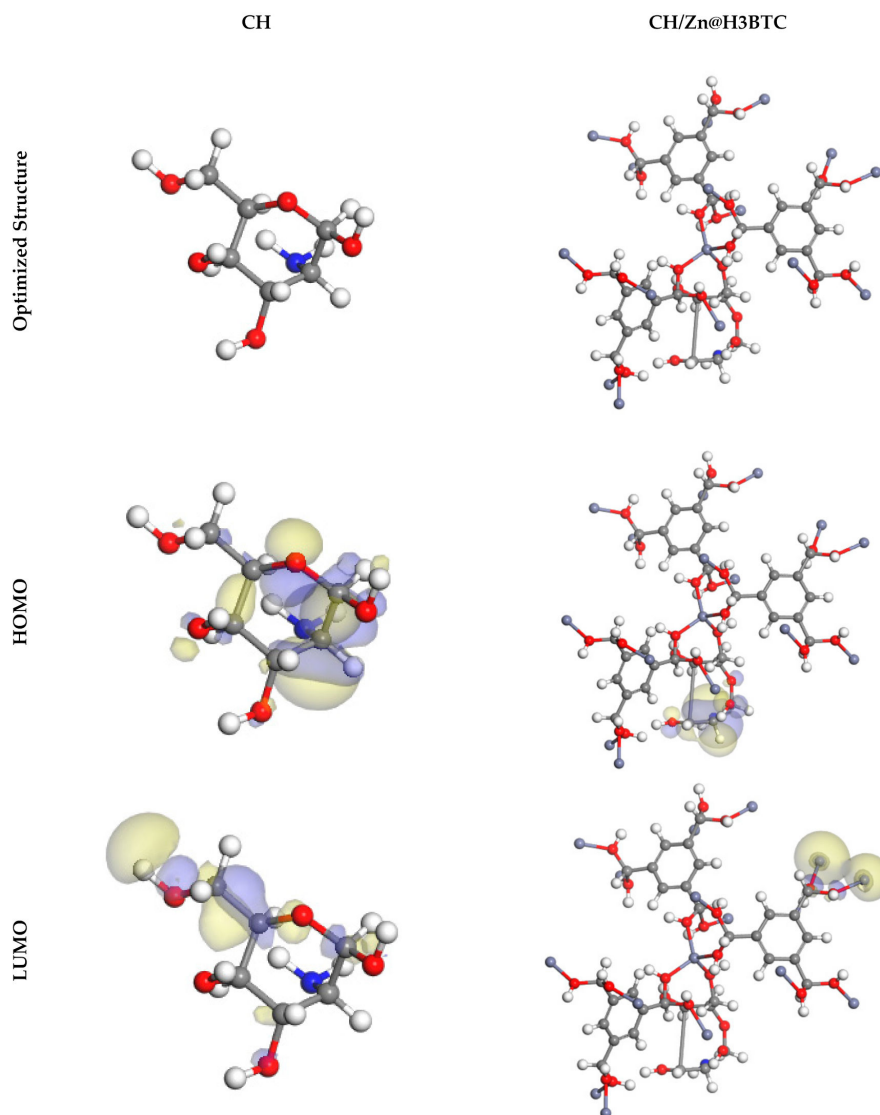


Figure 13. The molecular structures, HOMO, and LUMO of the monomer structures of CH and CH/Zn@H₃BTC optimized using the DMol3 module.

Table 3. The calculated quantum chemical parameters for the monomer structures of CH and CH/Zn@H₃BTC.

Inhibitor	CH	CH/Zn@H ₃ BTC
E_{HOMO} , eV	−5.00	−9.11
E_{LUMO} , eV	0.81	−8.57
ΔE , eV	5.80	0.55
I	5.00	9.11
A	−0.81	8.57
χ	2.09	8.84
η	2.90	0.27
σ	0.34	3.66
Dipole moment value, Debye	6.09	53.16
Molecular surface area, Å ²	193.50	1188.75

Most common inhibitors demonstrate relatively low electronegativity (χ) values, indicating their ability to offer electrons to a metal surface [61]. In contrast, high electronegativity (χ) values indicate the strong ability of the inhibitor molecule to attract and take electrons from metal surface atoms (i.e., back-donation) and form a stronger bond with metal atoms [62]. From the computed outcomes listed in Table 3, we found that the electronegativity of CH/Zn@H₃BTC is greater than that of CH. Consequently, CH/Zn@H₃BTC demonstrated superior electron admission ability compared to CH [63]. Additionally, the stability and susceptibility of a compound can be evaluated from hardness (η) and softness (σ) values, i.e., soft compounds have stronger protection ability than hard compounds due to the integrity created by the smooth coating of electrons on the steel exterior during the adsorption, thus indicating efficient protective inhibitors [52]. As shown in Table 3, CH/Zn@H₃BTC tended to have lower η values and higher σ values than CH, showing the strong ability to inhibit the donation of electrons to the examined steel, resulting in a strong anticorrosion ability.

The dipole moment is a vital indicator used to predict the prohibition effectiveness of a material [64]. The increase in dipole moment produced increases in deformation energy and molecule adsorption on the examined steel. Thus, the increases in dipole moment produced an increase in the corrosion inhibition potency [65]. As shown in Table 3, CH/Zn@H₃BTC had a greater dipole moment value (53.16 Debye) than CH (6.09 Debye), which verified the strong tendency for CH/Zn@H₃BTC to be adsorbed on steel and enhance the prohibition efficiency.

The ability of the examined particles to preserve the steel surface in the corrosive medium is related to their molecular surface area. The corrosion prohibition effectiveness increased as the molecular configuration increased because of the area over which the inhibitor molecules interacted with the steel surface increased. As shown in Table 3, CH/Zn@H₃BTC had the largest molecular surface area, which supports the experimental data; the corrosion prohibition potency was higher for CH/Zn@H₃BTC (1188.75 Å²) than for CH (193.50 Å²).

We used molecular electrostatic potential mapping (MEP) to investigate the higher-energy areas on CH/Zn@H₃BTC and CH molecules. MEP mapping is a 3D visual descriptor used to recognize the total electrostatic effect on a molecule by the total charge distribution [66]. In the MEP maps shown in Figure 14, the red indicates the highest electron density; the MEP is always more negative (nucleophilic reaction). The blue indicates the highest positive region (electrophilic reaction) [67]. An optical examination of Figure 14 shows that the greatest negative regions were mostly above O and N atoms; however, lower electron density can be observed over the Zn atoms and phenyl moieties in the investigated molecules. These positions with high electron density (i.e., red areas) in the investigated

molecules are the best sites for interactions within steel for fabricating a strongly adsorbed protective film.

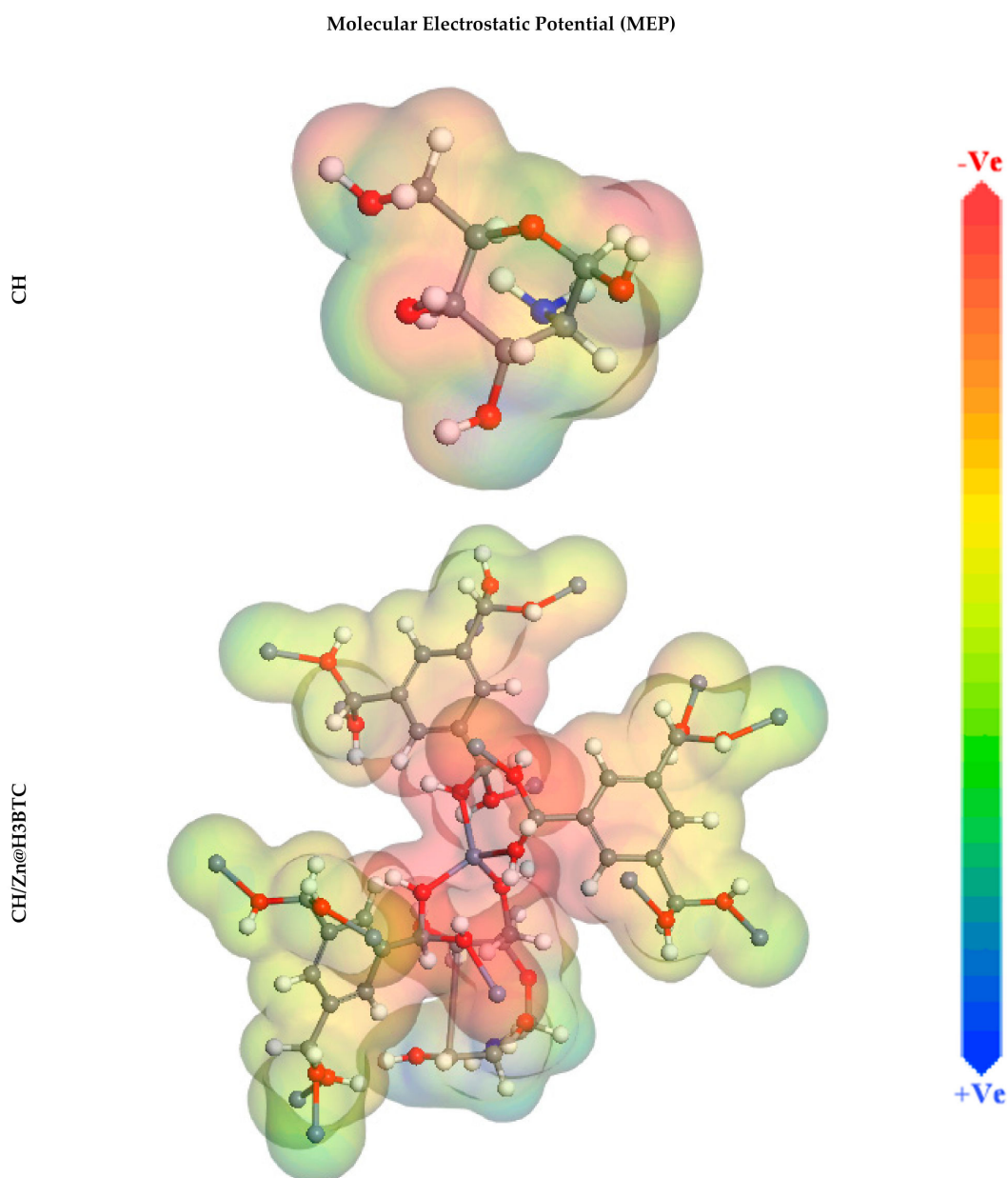


Figure 14. Graphical presentation of the MEP of the monomer structures of CH and CH/Zn@H₃BTC created using the DMol3 module.

3.6. MC Simulations

MC simulations were used to describe the adsorption mechanism and the correlations of the examined molecules with the steel surface. Figure 15 reveals the highest appropriate adsorption formations for the CH and CH/Zn@H₃BTC molecules on the steel surface produced with the adsorption locator module; they present an almost flat disposition, signifying an improvement in the adsorption and maximum surface coverage [68]. Moreover, the results of the adsorption energies from the MC simulations are displayed in Table 4. The data revealed that CH/Zn@H₃BTC ($-9676.99 \text{ kcal mol}^{-1}$) has a greater negative adsorption energy value than CH ($-3045.58 \text{ kcal mol}^{-1}$), indicating the powerful adsorption of CH/Zn@H₃BTC on the steel surface, creating a strongly adsorbed barrier that inhibits the corrosion of steel. These obtained data agree with the experimental results [69].

Additionally, Table 4 shows that the energy adsorption value of CH/Zn@H₃BTC in the pre-geometry optimization stage, i.e., unrelaxed ($-4675.19 \text{ kcal mol}^{-1}$), was more negative than that of CH ($-2908.63 \text{ kcal mol}^{-1}$). In the post-geometry optimization stage, i.e., relaxed ($-5001 \text{ kcal mol}^{-1}$), the value was greater than that of CH ($-136.94 \text{ kcal mol}^{-1}$), indicating a stronger corrosion prohibition potency of CH/Zn@H₃BTC compared to CH.

Final Equilibrium Configurations

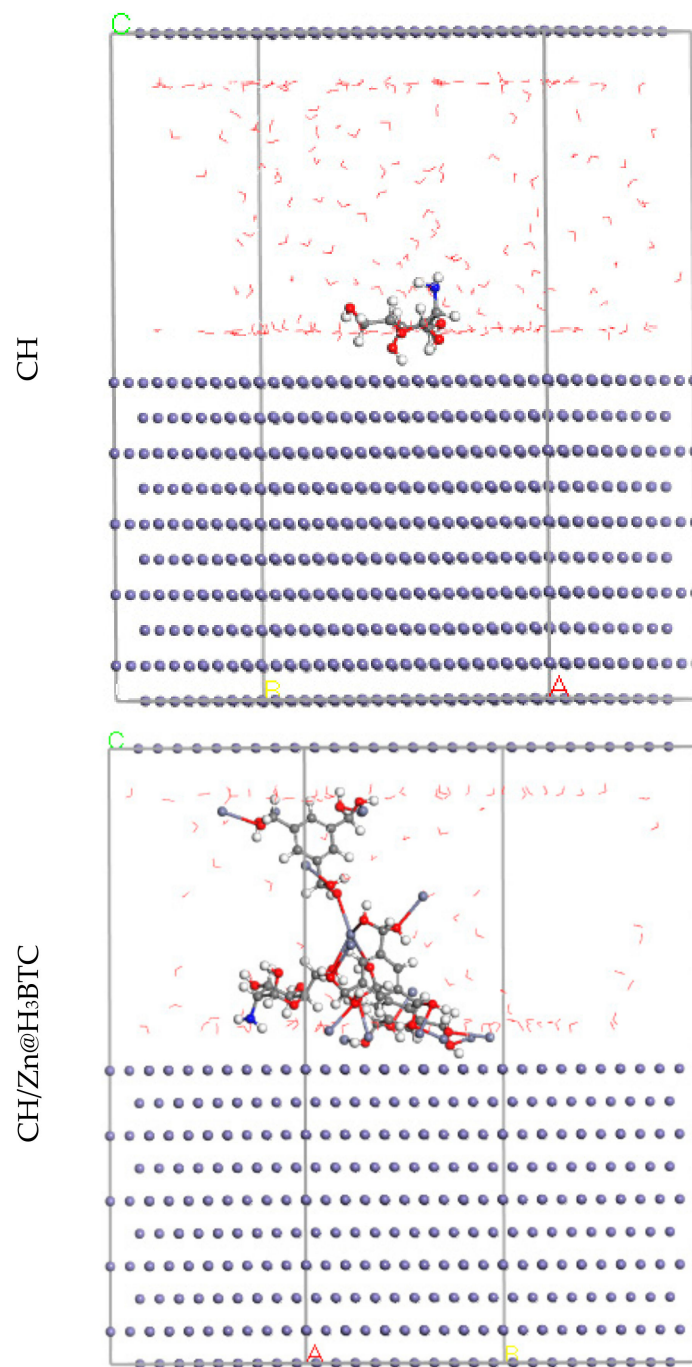


Figure 15. The most suitable configuration for adsorption of the monomer structures of CH and CH/Zn@H₃BTC on Fe (1 1 0) substrate obtained by adsorption locator module.

Table 4. Data and descriptors calculated by Mont Carlo (MC) simulation for adsorption of the monomer structures of CH and CH/Zn@H₃BTC on Fe (1 1 0).

Structures	Adsorption Energy kcal mol ⁻¹	Rigid Adsorption Energy kcal mol ⁻¹	Deformation Energy kcal mol ⁻¹	dE _{ads} /dN _i : Inhibitor kcal mol ⁻¹	dE _{ads} /dN _i : Water kcal mol ⁻¹
Fe (110)					
CH	−3045.58	−2908.63	−136.94	−103.40	−14.31
water					
Fe (110)					
CH/Zn@H ₃ BTC	−9676.99	−4675.19	−5001.80	−1388.29	−14.28
water					

The dE_{ads}/dN_i values explain the metal-adsorbates' structure energy if adsorbed when additives or water molecules are removed [70]. The dE_{ads}/dN_i value for CH/Zn@H₃BTC (−1388.29 kcal mol⁻¹) was found to be higher than that of CH (−103.40 kcal mol⁻¹), as presented in Table 4, which shows the good adsorption of CH/Zn@H₃BTC compare to CH. Furthermore, the water (dE_{ads}/dN_i) values are close (−14.30 kcal mol⁻¹), which is small compared to the CH/Zn@H₃BTC and CH values, revealing the strong adsorption of CH/Zn@H₃BTC and CH molecules compared to water molecules, which supports the exchanging of water molecules with CH/Zn@H₃BTC and CH molecules. Hence, the CH/Zn@H₃BTC and CH molecules are strongly adsorbed on the steel surface and form a preventive barrier, which prohibits corrosion of the steel surface in an acidic medium, as established by both experimental and computational examinations.

4. Conclusions

In this work, a novel composite of a zinc-based 1,3,5-benzenetricarboxylic acid framework Zn@H₃BTC coated with chitosan was synthesized via the solvothermal route. FTIR, FESEM, TGA, and BET analyses showed the successful impregnation of chitosan into Zn@H₃BTC. The fabricated CH/Zn@H₃BTC composite was compared to as effective inhibitors of D-steel corrosion in a sulfuric acid medium using empirical and computer simulation explorations. The results obtained from PDP and EIS are in good agreement. When CH and CH/Zn@H₃BTC concentrations were 200 ppm, the average inhibition capacity of PDP and EIS reached a maximum of 94.1% and 97.8%, and 91.8% and 94.3%, respectively. The PDP method showed that the anticorrosive action of CH/Zn@H₃BTC composite is dose-dependent, and its anticorrosion ability is achieved due to being a mixed type inhibitor. The j_{cor} value declined with the increase in the CH/Zn@H₃BTC composite dose. The R_{ct} at the interface of the metal/solution gradually increased as the CH/Zn@H₃BTC composite dose increased and the C_{dl} decreased owing to composite adsorption. CH/Zn@H₃BTC composite naturally adsorbed on the D steel interface, in agreement with the Langmuir isotherm model, which was considered combined physical-chemical adsorption. The FESEM pictures proved a smoother metal interface with the inclusion of 200 ppm CH and CH/Zn@H₃BTC composite compared to the blank medium without inhibitor, due to a compact CH/Zn@H₃BTC composite film forming on the D steel's surface. The mechanism of the protection process was confirmed by DFT and MD modeling methods. The computational modeling techniques substantiate the obtained empirical findings. The findings showed that CH/Zn@H₃BTC composite is an efficient inhibitor of steel corrosion in acidic corrosive solutions.

Author Contributions: M.G., investigation, supervision, methodology, resources, formal analysis, data curation, funding acquisition, writing—original draft, writing—review and editing; M.M.K., conceptualization, investigation, methodology, resources, formal analysis, data curation, funding acquisition, writing—original draft, writing—review and editing; K.S., conceptualization, investigation, methodology, resources, formal analysis, data curation, funding acquisition, writing—original draft, writing—review and editing; M.A.A.-O., writing—original draft, writing—review and editing; H.M.A.E.-L., conceptualization, supervision, investigation, methodology, resources, formal analysis, data curation, funding acquisition, writing—original draft, writing—review and editing. All authors have read and agreed to the published version of the manuscript.

Funding: This research was funded by King Faisal University, Al-Ahsa, Saudi Arabia, under research group project track (grant no. 1811004).

Institutional Review Board Statement: Not applicable.

Informed Consent Statement: Not applicable.

Data Availability Statement: The raw/processed data generated in this work are available upon request from the corresponding author.

Acknowledgments: The authors acknowledge the Deanship of Scientific Research at King Faisal University, Saudi Arabia, for financial support under research group project track (grant no. 1811004).

Conflicts of Interest: The authors declare no conflict of interest.

References

1. Ma, Q.; Luo, C.; Liu, S.; Li, H.; Wang, P.; Liu, D.; Lei, Y. Investigation of arc stability, microstructure evolution and corrosion resistance in underwater wet FCAW of duplex stainless steel. *J. Mater. Res. Technol.* **2021**, *15*, 5482–5495. [[CrossRef](#)]
2. Chugh, B.; Singh, A.K.; Thakur, S.; Pani, B.; Pandey, A.K.; Lgaz, H.; Chung, I.-M.; Ebenso, E.E. An Exploration about the Interaction of Mild Steel with Hydrochloric Acid in the Presence of N-(Benzo[d]thiazole-2-yl)-1-phenylethan-1-imines. *J. Phys. Chem. C* **2019**, *123*, 22897–22917. [[CrossRef](#)]
3. Singh, D.K.; Kumar, S.; Udayabhanu, G.; John, R.P. 4(N,N-dimethylamino) benzaldehyde nicotinic hydrazone as corrosion inhibitor for mild steel in 1 M HCl solution: An experimental and theoretical study. *J. Mol. Liq.* **2016**, *216*, 738–746. [[CrossRef](#)]
4. Wang, X.; Wang, B.; Wang, Q.; Li, R.; Liu, H.; Jiang, H.; Liu, J. Inhibition effect and adsorption behavior of two pyrimidine derivatives as corrosion inhibitors for Q235 steel in CO₂-saturated chloride solution. *J. Electroanal. Chem.* **2021**, *903*, 115827. [[CrossRef](#)]
5. Laabaissi, T.; Rbaa, M.; Benhiba, F.; Rouifi, Z.; Kumar, U.P.; Bentiss, F.; Oudda, H.; Lakhri, B.; Warad, I.; Zarrouk, A. Insight into the corrosion inhibition of new benzodiazepine derivatives as highly efficient inhibitors for mild steel in 1 M HCl: Experimental and theoretical study. *Colloids Surf. A Physicochem. Eng. Asp.* **2021**, *629*, 127428. [[CrossRef](#)]
6. Shamsa, A.; Barmatov, E.; Hughes, T.L.; Hua, Y.; Neville, A.; Barker, R. Hydrolysis of imidazoline based corrosion inhibitor and effects on inhibition performance of X65 steel in CO₂ saturated brine. *J. Pet. Sci. Eng.* **2022**, *208*, 109235. [[CrossRef](#)]
7. Yang, H.M. Role of organic and eco-friendly inhibitors on the corrosion mitigation of steel in acidic environments—A state-of-art review. *Molecules* **2021**, *26*, 3473. [[CrossRef](#)]
8. De Sousa Rodrigues, F.A.; Gonçalves, Y.M.H.; Horta, B.A.C.; da Silva Santos, I.; Silva, B.V.; D'Elia, E. Experimental and theoretical studies of isonitrosoacetanilides derivatives as corrosion inhibitors for mild steel in 1 mol L⁻¹ HCl. *J. Mol. Struct.* **2021**, *1245*, 131256. [[CrossRef](#)]
9. Rajeswari, V.; Kesavan, D.; Gopiraman, M.; Viswanathamurthi, P. Physicochemical studies of glucose, gellan gum, and hydroxypropyl cellulose—Inhibition of cast iron corrosion. *Carbohydr. Polym.* **2013**, *95*, 288–294. [[CrossRef](#)]
10. Mobin, M.; Rizvi, M. Inhibitory effect of xanthan gum and synergistic surfactant additives for mild steel corrosion in 1 M HCl. *Carbohydr. Polym.* **2016**, *136*, 384–393. [[CrossRef](#)] [[PubMed](#)]
11. Umoren, S.A.; Solomon, M.M.; Udoso, I.I.; Udoh, A.P. Synergistic and antagonistic effects between halide ions and carboxymethyl cellulose for the corrosion inhibition of mild steel in sulphuric acid solution. *Cellulose* **2010**, *17*, 635–648. [[CrossRef](#)]
12. Hefni, H.H.H.; Azzam, E.M.; Badr, E.A.; Hussein, M.; Tawfik, S.M. Synthesis, characterization and anticorrosion potentials of chitosan-g-PEG assembled on silver nanoparticles. *Int. J. Biol. Macromol.* **2016**, *83*, 297–305. [[CrossRef](#)]
13. Quraishi, M.A.; Chauhan, D.S.; Saji, V.S. Heterocyclic biomolecules as green corrosion inhibitors. *J. Mol. Liq.* **2021**, *341*, 117265. [[CrossRef](#)]
14. Chaubey, N.; Savita; Quraishi, A.; Chauhan, D.S.; Quraishi, M.A. Frontiers and advances in green and sustainable inhibitors for corrosion applications: A critical review. *J. Mol. Liq.* **2021**, *321*, 114385. [[CrossRef](#)]
15. Al Obeidli, A.; Ben Salah, H.; Al Murisi, M.; Sabouni, R. Recent advancements in MOFs synthesis and their green applications. *Int. J. Hydrogen Energy* **2021**. [[CrossRef](#)]

16. Nguyen Thi, H.P.; Ninh, H.D.; Tran, C.; Van Le, B.T.; Bhosale, S.V.; La, D.D. Size-Control and Surface Modification of Flexible Metal-Organic Framework MIL-53(Fe) by Polyethyleneglycol for 5-Fluorouracil Anticancer Drug Delivery. *ChemistrySelect* **2019**, *4*, 2333–2338. [CrossRef]
17. Zheng, J.; Cui, X.; Yang, Q.; Ren, Q.; Yang, Y.; Xing, H. Shaping of ultrahigh-loading MOF pellet with a strongly anti-tearing binder for gas separation and storage. *Chem. Eng. J.* **2018**, *354*, 1075–1082. [CrossRef]
18. Barbosa, P.F.P.; Cumba, L.R.; Andrade, R.D.A.; do Carmo, D.R. Chemical Modifications of Cyclodextrin and Chitosan for Biological and Environmental Applications: Metals and Organic Pollutants Adsorption and Removal. *J. Polym. Environ.* **2019**, *27*, 1352–1366. [CrossRef]
19. Qin, X.; Huang, Y.; Wang, K.; Xu, T.; Wang, Y.; Liu, P.; Kang, Y.; Zhang, Y. Novel hierarchically porous Ti-MOFs/nitrogen-doped graphene nanocomposite served as high efficient oxygen reduction reaction catalyst for fuel cells application. *Electrochim. Acta* **2019**, *297*, 805–813. [CrossRef]
20. Kaur, R.; Sharma, A.L.; Kim, K.-H.; Deep, A. A novel CdTe/Eu-MOF photoanode for application in quantum dot-sensitized solar cell to improve power conversion efficiency. *J. Ind. Eng. Chem.* **2017**, *53*, 77–81. [CrossRef]
21. Zhang, Y.; Yang, X.; Zhou, H.-C. Synthesis of MOFs for heterogeneous catalysis via linker design. *Polyhedron* **2018**, *154*, 189–201. [CrossRef]
22. Zhan, K.; Zhu, Y.; Yan, J.; Chen, Y. Enhanced-performance relative humidity sensor based on MOF-801 photonic crystals. *Phys. Lett. A* **2020**, *384*, 126678. [CrossRef]
23. Liu, Y.; Wang, Y.; Chen, Y.; Wang, C.; Guo, L. NiCo-MOF nanosheets wrapping polypyrrole nanotubes for high-performance supercapacitors. *Appl. Surf. Sci.* **2020**, *507*, 145089. [CrossRef]
24. Abánades Lázaro, I.; Forgan, R.S. Application of zirconium MOFs in drug delivery and biomedicine. *Coord. Chem. Rev.* **2019**, *380*, 230–259. [CrossRef]
25. Hassan, M.A.; Tamer, T.M.; Valachová, K.; Omer, A.M.; El-Shafeey, M.; Eldin, M.S.M.; Šoltés, L. Antioxidant and antibacterial polyelectrolyte wound dressing based on chitosan/hyaluronan/phosphatidylcholine dihydroquercetin. *Int. J. Biol. Macromol.* **2021**, *166*, 18–31. [CrossRef]
26. Omer, A.M.; Ziora, Z.M.; Tamer, T.M.; Khalifa, R.E.; Hassan, M.A.; Mohy-Eldin, M.S.; Blaskovich, M.A. Formulation of quaternized aminated chitosan nanoparticles for efficient encapsulation and slow release of curcumin. *Molecules* **2021**, *26*, 449. [CrossRef] [PubMed]
27. Hassan, M.A.; Omer, A.M.; Abbas, E.; Baset, W.M.; Tamer, T.M. Preparation, physicochemical characterization and antimicrobial activities of novel two phenolic chitosan Schiff base derivatives. *Sci. Rep.* **2018**, *8*, 11416. [CrossRef]
28. Han, W.; Huang, X.; Lu, G.; Tang, Z. Research Progresses in the Preparation of Co-based Catalyst Derived from Co-MOFs and Application in the Catalytic Oxidation Reaction. *Catal. Surv. Asia* **2018**, *23*, 64–89. [CrossRef]
29. Altaf, M.; Sohail, M.; Mansha, M.; Iqbal, N.; Sher, M.; Fazal, A.; Ullah, N.; Isab, A.A. Synthesis, Characterization, and Photoelectrochemical Catalytic Studies of a Water-Stable Zinc-Based Metal–Organic Framework. *ChemSusChem* **2018**, *11*, 542–546. [CrossRef]
30. Wang, Z.; Jin, Z.; Yang, H.; Ma, X.; Liu, H. Synergistic interface phenomena between MOFs, NiPx for efficient hydrogen production. *Mol. Catal.* **2019**, *467*, 78–86. [CrossRef]
31. Nazir, M.H.; Khan, Z.A.; Saeed, A.; Siddaiah, A.; Menezes, P.L. Synergistic wear-corrosion analysis and modelling of nanocomposite coatings. *Tribol. Int.* **2018**, *121*, 30–44. [CrossRef]
32. Yang, D.; Yang, G.; Gai, S.; He, F.; Li, C.; Yang, P. Multifunctional Theranostics for Dual-Modal Photodynamic Synergistic Therapy via Stepwise Water Splitting. *ACS Appl. Mater. Interfaces* **2017**, *9*, 6829–6838. [CrossRef] [PubMed]
33. Ramezanzadeh, M.; Ramezanzadeh, B.; Mahdavian, M.; Bahlakeh, G. Development of metal-organic framework (MOF) decorated graphene oxide nanoplateforms for anti-corrosion epoxy coatings. *Carbon* **2020**, *161*, 231–251. [CrossRef]
34. Cao, K.; Yu, Z.; Yin, D.; Chen, L.; Jiang, Y.; Zhu, L. Fabrication of BTA-MOF-TEOS-GO nanocomposite to endow coating systems with active inhibition and durable anticorrosion performances. *Prog. Org. Coatings* **2020**, *143*, 105629. [CrossRef]
35. Furukawa, H.; Yaghi, O.M. Storage of Hydrogen, Methane, and Carbon Dioxide in Highly Porous Covalent Organic Frameworks for Clean Energy Applications. *J. Am. Chem. Soc.* **2009**, *131*, 8875–8883. [CrossRef]
36. ASTM License Agreement G3–89A, Standard Practice for Conventions Applicable to Electrochemical Measurements in Corrosion Testing. 2010. pp. 1–9. Available online: <https://www.document-center.com/standards/show/ASTM-G3> (accessed on 5 January 2021).
37. Abd El-Lateef, H.M.; Sayed, A.R.; Shalabi, K. Synthesis and theoretical studies of novel conjugated polyazomethines and their application as efficient inhibitors for C1018 steel pickling corrosion behavior. *Surf. Interfaces* **2021**, *23*, 101037. [CrossRef]
38. Abd El-Lateef, H.M.; Shalabi, K.; Abdelhamid, A.A. One-pot synthesis of novel triphenyl hexyl imidazole derivatives catalyzed by ionic liquid for acid corrosion inhibition of C1018 steel: Experimental and computational perspectives. *J. Mol. Liq.* **2021**, *334*, 116081. [CrossRef]
39. Chafiq, M.; Chaouiki, A.; Al-Hadeethi, M.R.; Ali, I.H.; Mohamed, S.K.; Toumiat, K.; Salghi, R. Naproxen-Based Hydrazones as Effective Corrosion Inhibitors for Mild Steel in 1.0 M HCl. *Coatings* **2020**, *10*, 700. [CrossRef]
40. Khamaysa, O.M.A.; Selatnia, I.; Zeghache, H.; Lgaz, H.; Sid, A.; Chung, I.-M.; Benahmed, M.; Gherraf, N.; Mosset, P. Enhanced corrosion inhibition of carbon steel in HCl solution by a newly synthesized hydrazone derivative: Mechanism exploration from electrochemical, XPS, and computational studies. *J. Mol. Liq.* **2020**, *315*, 113805. [CrossRef]

41. Chaouiki, A.; Chafiq, M.; Lgaz, H.; Al-Hadeethi, M.R.; Ali, I.H.; Masroor, S.; Chung, I.-M. Green Corrosion Inhibition of Mild Steel by Hydrazone Derivatives in 1.0 M HCl. *Coatings* **2020**, *10*, 640. [[CrossRef](#)]
42. Chai, C.; Xu, Y.; Shi, S.; Zhao, X.; Wu, Y.; Xu, Y.; Zhang, L. Functional polyaspartic acid derivatives as eco-friendly corrosion inhibitors for mild steel in 0.5 M H₂SO₄ solution. *RSC Adv.* **2018**, *8*, 24970–24981. [[CrossRef](#)]
43. Gao, L.; Peng, S.; Gong, Z.; Chen, J. A combination of experiment and theoretical methods to study the novel and low-cost corrosion inhibitor 1-hydroxy-7-azabenzotriazole for mild steel in 1 M sulfuric acid. *RSC Adv.* **2018**, *8*, 38506–38516. [[CrossRef](#)]
44. Lgaz, H.; Salghi, R.; Masroor, S.; Kim, S.-H.; Kwon, C.; Kim, S.Y.; Yang, Y.-J.; Chung, I.-M. Assessing corrosion inhibition characteristics of hydrazone derivatives on mild steel in HCl: Insights from electronic-scale DFT and atomic-scale molecular dynamics. *J. Mol. Liq.* **2020**, *308*, 112998. [[CrossRef](#)]
45. El-Lateef, H.M.A. Corrosion inhibition characteristics of a novel salicylidene isatin hydrazine sodium sulfonate on carbon steel in HCl and a synergistic nickel ions additive: A combined experimental and theoretical perspective. *Appl. Surf. Sci.* **2020**, *501*, 144237. [[CrossRef](#)]
46. Tantawy, A.H.; Soliman, K.A.; Abd El-Lateef, H.M. Experimental and computational approaches of sustainable quaternary bisammonium fluorosurfactants for corrosion inhibition as protective films at mild steel/H₂SO₄ interface. *Colloids Surf. A Physicochem. Eng. Asp.* **2021**, *614*, 126141. [[CrossRef](#)]
47. Tantawy, A.H.; Soliman, K.A.; Abd El-Lateef, H.M. Novel synthesized cationic surfactants based on natural piper nigrum as sustainable-green inhibitors for steel pipeline corrosion in CO₂-3.5%NaCl: DFT, Monte Carlo simulations and experimental approaches. *J. Clean. Prod.* **2020**, *250*, 119510. [[CrossRef](#)]
48. Kaya, S.; Guo, L.; Kaya, C.; Tüzün, B.; Obot, I.B.; Tourir, R.; Islam, N. Quantum chemical and molecular dynamic simulation studies for the prediction of inhibition efficiencies of some piperidine derivatives on the corrosion of iron. *J. Taiwan Inst. Chem. Eng.* **2016**, *65*, 522–529. [[CrossRef](#)]
49. Khalaf, M.M.; Tantawy, A.H.; Soliman, K.A.; Abd El-Lateef, H.M. Cationic gemini-surfactants based on waste cooking oil as new 'green' inhibitors for N80-steel corrosion in sulphuric acid: A combined empirical and theoretical approaches. *J. Mol. Struct.* **2020**, *1203*, 127442. [[CrossRef](#)]
50. Saleh, M.M.; Mahmoud, M.G.; Abd El-Lateef, H.M. Comparative study of synergistic inhibition of mild steel and pure iron by 1-hexadecylpyridinium chloride and bromide ions. *Corros. Sci.* **2019**, *154*, 70–79. [[CrossRef](#)]
51. Abd El-Lateef, H.M.; Mohamed, I.M.A.; Zhu, J.-H.; Khalaf, M.M. An efficient synthesis of electrospun TiO₂-nanofibers/Schiff base phenylalanine composite and its inhibition behavior for C-steel corrosion in acidic chloride environments. *J. Taiwan Inst. Chem. Eng.* **2020**, *112*, 306–321. [[CrossRef](#)]
52. Abd El-Lateef, H.M.; Shalabi, K.; Tantawy, A.H. Corrosion inhibition of carbon steel in hydrochloric acid solution using newly synthesized urea-based cationic fluorosurfactants: Experimental and computational investigations. *New J. Chem.* **2020**, *44*, 17791–17814. [[CrossRef](#)]
53. Ansari, K.R.; Quraishi, M.A.; Singh, A.; Ramkumar, S.; Obote, I.B. Corrosion inhibition of N80 steel in 15% HCl by pyrazolone derivatives: Electrochemical, surface and quantum chemical studies. *RSC Adv.* **2016**, *6*, 24130–24141. [[CrossRef](#)]
54. Masroor, S.; Mobin, M.; Alam, M.J.; Ahmad, S. The novel iminium surfactant p-benzylidene benzyl dodecyl iminium chloride as a corrosion inhibitor for plain carbon steel in 1 M HCl: Electrochemical and DFT evaluation. *RSC Adv.* **2017**, *7*, 23182–23196. [[CrossRef](#)]
55. Gadow, H.S.; Motawea, M.M. Investigation of the corrosion inhibition of carbon steel in hydrochloric acid solution by using ginger roots extract. *RSC Adv.* **2017**, *7*, 24576–24588. [[CrossRef](#)]
56. Alam, R.; Mobin, M.; Aslam, J. Investigation of anti-corrosive properties of poly(aniline-co-2-pyridylamine-co-2,3-xylylidine) and its nanocomposite poly(aniline-co-2-pyridylamine-co-2,3-xylylidine)/ZnO on mild steel in 0.1 M HCl. *Appl. Surf. Sci.* **2016**, *368*, 360–367. [[CrossRef](#)]
57. Singh, A.; Ansari, K.R.; Haque, J.; Dohare, P.; Lgaz, H.; Salghi, R.; Quraishi, M.A. Effect of electron donating functional groups on corrosion inhibition of mild steel in hydrochloric acid: Experimental and quantum chemical study. *J. Taiwan Inst. Chem. Eng.* **2018**, *82*, 233–251. [[CrossRef](#)]
58. Ashassi-Sorkhabi, H.; Nabavi-Amri, S.A. Polarization and impedance methods in corrosion inhibition study of carbon steel by amines in petroleum–water mixtures. *Electrochim. Acta* **2002**, *47*, 2239–2244. [[CrossRef](#)]
59. Boulhaoua, M.; El Hafi, M.; Zehra, S.; Eddaif, L.; Alrashdi, A.A.; Lahmidi, S.; Guo, L.; Mague, J.T.; Lgaz, H. Synthesis, structural analysis and corrosion inhibition application of a new indazole derivative on mild steel surface in acidic media complemented with DFT and MD studies. *Colloids Surfaces A Physicochem. Eng. Asp.* **2021**, *617*, 126373. [[CrossRef](#)]
60. Abd El-Lateef, H.M.; Shalabi, K.; Tantawy, A.H. Corrosion inhibition and adsorption features of novel bioactive cationic surfactants bearing benzenesulphonamide on C1018-steel under sweet conditions: Combined modeling and experimental approaches. *J. Mol. Liq.* **2020**, *320*, 114564. [[CrossRef](#)]
61. Palaniappan, N.; Cole, I.S.; Kuznetsov, A.E. Experimental and computational studies of graphene oxide covalently functionalized by octylamine: Electrochemical stability, hydrogen evolution, and corrosion inhibition of the AZ13 Mg alloy in 3.5% NaCl. *RSC Adv.* **2020**, *10*, 11426–11434. [[CrossRef](#)]
62. Abd El-Lateef, H.M.; Shaaban, S.; Khalaf, M.M.; Toghan, A.; Shalabi, K. Synthesis, Experimental, and Computational Studies of Water Soluble Anthranilic Organoselenium Compounds as Safe Corrosion Inhibitors for J55 Pipeline Steel in Acidic Oilfield Formation Water. *Colloids Surf. A Physicochem. Eng. Asp.* **2021**, *625*, 126894. [[CrossRef](#)]

63. Upadhyay, A.; Purohit, A.K.; Mahakur, G.; Dash, S.; Kar, P.K. Verification of corrosion inhibition of Mild steel by some 4-Aminoantipyrine-based Schiff bases—Impact of adsorbate substituent and cross-conjugation. *J. Mol. Liq.* **2021**, *333*, 115960. [[CrossRef](#)]
64. Oyebamiji, A.K.; Adeleke, B.B. Quantum chemical studies on inhibition activities of 2,3-dihydroxypropyl-sulfanyl derivative on carbon steel in acidic media. *Int. J. Corros. Scale Inhib.* **2018**, *7*, 498–508. [[CrossRef](#)]
65. Singh, A.; Ansari, K.R.; Quraishi, M.A.; Kaya, S. Theoretically and experimentally exploring the corrosion inhibition of N80 steel by pyrazol derivatives in simulated acidizing environment. *J. Mol. Struct.* **2020**, *1206*, 127685. [[CrossRef](#)]
66. Hegazy, M.A.; Hegazy, M.M.; Awad, M.K.; Shawky, M. Chemical, electrochemical, theoretical (DFT & MEP), thermodynamics and surface morphology studies of carbon steel during gas and oil production using three novel di-cationic amphiphilic corrosion inhibitors in acidic medium. *J. Mol. Liq.* **2021**, *337*, 116541. [[CrossRef](#)]
67. Abd El-Lateef, H.M.; Shalabi, K.; Sayed, A.R.; Gomha, S.M.; Bakir, E.M. The novel polythiadiazole polymer and its composite with α -Al(OH)₃ as inhibitors for steel alloy corrosion in molar H₂SO₄: Experimental and computational evaluations. *J. Ind. Eng. Chem.* **2022**, *105*, 238–250. [[CrossRef](#)]
68. Shalabi, K.; Helmy, A.M.; El-Askalany, A.H.; Shahba, M.M. New pyridinium bromide mono-cationic surfactant as corrosion inhibitor for carbon steel during chemical cleaning: Experimental and theoretical studies. *J. Mol. Liq.* **2019**, *293*, 111480. [[CrossRef](#)]
69. El Aaad, H.; Galai, M.; Ouakki, M.; Elgendy, A.; Touhami, M.E.; Chahine, A. Improvement of the corrosion resistance of mild steel in sulfuric acid by new organic-inorganic hybrids of Benzimidazole-Pyrophosphate: Facile synthesis, characterization, experimental and theoretical calculations (DFT and MC). *Surf. Interfaces* **2021**, *24*, 101084. [[CrossRef](#)]
70. Dehghani, A.; Mostafatabar, A.H.; Bahlakeh, G.; Ramezanzadeh, B. A detailed study on the synergistic corrosion inhibition impact of the Quercetin molecules and trivalent europium salt on mild steel; electrochemical/surface studies, DFT modeling, and MC/MD computer simulation. *J. Mol. Liq.* **2020**, *316*, 113914. [[CrossRef](#)]